

1 **Increasing resolution and resolving convection improves**
2 **the simulation of cloud-radiative effects over the North**
3 **Atlantic**

4 **Fabian Senf¹, Aiko Voigt^{2,3}, Nicolas Clerbaux⁴, Anja Hünerbein¹, Hartwig**
5 **Deneke¹**

6 ¹Leibniz Institute for Tropospheric Research, Leipzig

7 ²Institute for Meteorology and Climate Research - Department Troposphere Research, Karlsruhe Institute
8 of Technology, Karlsruhe

9 ³Lamont-Doherty Earth Observatory, Columbia University, New York, USA

10 ⁴Royal Meteorological Institute of Belgium, Brussels

11 **Key Points:**

- 12 • biases in cloud-radiative effects become smaller as grid spacing is decreased, es-
13 pecially from 80 to 20 km
- 14 • refinements down to 2.5 km substantially reduce shortwave CRE biases only when
15 the convection scheme is disabled
- 16 • compensating biases between longwave and shortwave become smaller for finer res-
17 olutions leading to more realistic radiation fluxes

Corresponding author: Fabian Senf, senf@tropos.de

Abstract

Clouds interact with atmospheric radiation and substantially modify the Earth's energy budget. Cloud formation processes occur over a vast range of spatial and temporal scales which make their thorough numerical representation challenging. Therefore, the impact of parameter choices for simulations of cloud-radiative effects is assessed in the current study. Numerical experiments were carried out using the ICOSahedral Nonhydrostatic (ICON) model with varying grid spacings between 2.5 and 80 km and with different subgrid-scale parameterization approaches. Simulations have been performed over the North Atlantic with either one-moment or two-moment microphysics and with convection being parameterized or explicitly resolved by grid-scale dynamics. Simulated cloud-radiative effects are compared to products derived from Meteosat measurements. Furthermore, a sophisticated cloud classification algorithm is applied to understand the differences and dependencies of simulated and observed cloud-radiative effects. The cloud classification algorithm developed for the satellite observations is also applied to the simulation output based on synthetic infrared brightness temperatures, a novel approach that is not impacted by changing insolation and guarantees a consistent and fair comparison. It is found that flux biases originate equally from clear-sky and cloudy parts of the radiation field. Simulated cloud amounts and cloud-radiative effects are dominated by marine, shallow clouds, and their behaviour is highly resolution dependent. Bias compensation between shortwave and longwave flux biases, seen in the coarser simulations, is significantly diminished for higher resolutions. Based on the analysis results, it is argued that cloud-microphysical and cloud-radiative properties have to be adjusted to further improve agreement with observed cloud-radiative effects.

Plain Language Summary

Clouds are a major challenge for climate science and their effects are difficult to quantify. Clouds scatter sunlight back into space and thus prevent the Earth from warming up. But clouds also hold back heat radiation upwelling from the surface. Both effects typically compensate each other and thus lead to the net cloud-radiative effect. Computer programs that are used to simulate the climate - so-called climate models - often use very coarse grid-box sizes in their computational mesh. Cloud processes and their effects are represented in them in a very simplified way, which leads to problems. For this reason, this study deals with the question to what extent the simulations of cloud-radiative effects can be improved by choosing more precise descriptions of the cloud processes. To investigate this, different configurations of more realistic models were taken to simulate cloud formation over the North Atlantic. The resulting simulation data were compared to satellite observations. It could be shown that problematic biases of the coarser climate models are reduced if, as is usual in weather models, one switches to smaller grid-box sizes and improved descriptions of the cloud processes.

1 Introduction

Clouds are very effective in cooling the Earth. Clouds scatter sunlight back to space before it can be absorbed by the Earth's surface. They also trap longwave radiation originating from the warm surface and thus induce a counter-acting greenhouse effect (Ramanathan et al., 1989). In the global mean, the shortwave effect of clouds (-46 to -48 W m^{-2}) dominates over their longwave effect (26 to 28 W m^{-2}) in the top-of-the-atmosphere (TOA) radiation budget, leading to a net negative cloud-radiative effect (CRE) of -18 to -20 W m^{-2} (Arking, 1991; G. L. Stephens et al., 2012; Henderson et al., 2013; Zelinka et al., 2017). The magnitude of net radiative effects becomes even larger and more important for cloud systems over the mid-latitude oceans, where the net CRE is more than twice the global average (see e.g. Zelinka et al., 2017).

67 Cloud feedbacks, i.e. the impact of changes in clouds on the TOA radiation bud-
68 get, remain a major source of uncertainty in future climate projections (Boucher et al.,
69 2013; Ceppi et al., 2017). Recent work indicates that the global-mean cloud feedback to
70 global warming is likely positive, i.e., cloud changes will lead to an additional warming
71 (Ceppi et al., 2017). This is largely attributed to a reduction in low-level cloud amount
72 and a rise of high-level clouds (Zelinka et al., 2017). Yet, significant uncertainties remain
73 in the parameterization of clouds and their radiative effects, in particular regarding the
74 treatment of cloud microphysical processes in climate models (Gettelman & Sherwood,
75 2016). Understanding clouds and their radiative changes is also relevant for regional cli-
76 mate change, as the simulated response of the atmospheric circulation to global warm-
77 ing is strongly shaped by clouds (Voigt & Shaw, 2015; Voigt et al., 2019; Ceppi & Shep-
78 herd, 2017).

79 The steady increase in computational power and advent of a new generation of mod-
80 els that can harness this power has begun to allow for global atmospheric simulations
81 with horizontal grid spacings on the order of a few kilometers (e.g. Satoh et al., 2018;
82 Stevens et al., 2019). In these high-resolution simulations, clouds and the atmospheric
83 flow interact much more naturally than in current low-resolution models typically run
84 horizontal grid spacings of around 50 km. The explicit simulation of at least part of the
85 cloud-scale circulations in fact provides a physical link between the resolved atmospheric
86 flow and the parameterized cloud-microphysical processes (Satoh et al., 2019; Stevens
87 et al., 2020). Moreover, and importantly, high-resolution models and satellite observa-
88 tions probe the atmosphere on similar spatial and temporal scales, allowing for a mean-
89 ingful comparison between simulation and observations that helps model evaluation as
90 well as the interpretation of observations (Satoh et al., 2019). As such, high-resolution
91 modelling might break the so-called cloud parameterization "deadlock" (Randall et al.,
92 2003) and promises to lead to more reliable simulations of cloud and precipitation re-
93 sponses to future climate change (Roberts et al., 2018; Collins et al., 2018; Stevens et
94 al., 2020).

95 Motivated by these advances, we consider the radiative effects of mid-latitude cloud
96 systems in simulations with a large range of horizontal resolutions, with three different
97 treatments of atmospheric convection, and with two different treatments of cloud micro-
98 physics in this study. This creates a hierarchy of simulations that at the one end resem-
99 bles current low-resolution climate models with parameterized convection and relatively
100 simple cloud microphysics, and at the other end resembles the next-generation high-resolution
101 models with explicit convection and more detailed cloud microphysics. Through this ap-
102 proach we investigate how a sequential reduction in model grid spacing from climate-
103 model scales of 80 km down to 2.5 km affects, and hopefully improves, the simulation
104 of cloud-radiative effects. Furthermore, we investigate the impact of subgrid-scale pa-
105 rameterization choices regarding convection (fully explicit convection vs. parameterized
106 shallow convection vs. parameterized convection) and cloud microphysics (one-moment
107 scheme vs. two-moment scheme) on cloud-radiative effects and the radiation budget. To
108 this end we analyze simulations with the ICOSahedral Nonhydrostatic (ICON) model
109 (Zängl et al., 2014) over a large domain of the North Atlantic. Our work contributes to
110 recent efforts to understand the sensitivity of climate simulations with respect to hor-
111 izontal resolution and convection parameterization (Webb et al., 2015; Haarsma et al.,
112 2016; Evans et al., 2017; Maher et al., 2018; Thomas et al., 2018; Vannière et al., 2019).
113 We expand these efforts by bridging the gap between current climate models and
114 convection-permitting models.

115 The focus region of this study is the mid-latitude North Atlantic. This is motivated
116 on the one hand by its importance for current and future European weather, and on the
117 other hand by the difficulties of current coarse-resolution global climate models to rep-
118 resent the radiative effects of mid-latitude clouds (Bodas-Salcedo et al., 2014; Voigt et
119 al., 2019) and their coupling to the circulation (Grise & Polvani, 2014). Cloud-radiative

120 effects in the mid-latitudes feed back onto circulations. As such, they are essential to an-
 121 ticipated poleward shift and strengthening of the eddy-driven jet streams under global
 122 warming (Voigt & Shaw, 2016; Albern et al., 2019; Ceppi & Hartmann, 2016; Li et al.,
 123 2019), and they also can impact mid-latitude weather on time-scales of days (Schäfer &
 124 Voigt, 2018; Grise et al., 2019)

125 Biases in simulated mid-latitude CREs appear to be primarily due to deficiencies
 126 in parameterized physics of clouds and convection (Ceppi & Hartmann, 2015). These physics
 127 strongly depend on cloud type. Analysis of data from space-born imaging radiometers
 128 has shown that low-level clouds over the oceans provide the largest contribution to the
 129 net TOA CREs because reflection of sunlight dominates over the trapping of longwave
 130 radiation (Hartmann et al., 1992; Ockert-Bell & Hartmann, 1992; Chen et al., 2000). The
 131 traditional cloud classification approaches have been revised to assess the importance
 132 of cloud regimes as a whole using clustering techniques (Oreopoulos & Rossow, 2011; Ore-
 133 opoulos et al., 2016; McDonald & Parsons, 2018) and the vertical structure of cloud fields
 134 based on active satellite sensors (G. Stephens et al., 2018; L’Ecuyer et al., 2019). The
 135 latter showed that clouds are predominantly organized in multiple layers, which is typ-
 136 ically not resolved by passive imagery. Because active satellite observations are very sparse
 137 in time and space, we here nevertheless rely on the traditional cloud classification ap-
 138 proach to separate cloud-cover and CRE model biases into contributions from different
 139 cloud types. The comparison is based on instantaneous and high-resolution geostation-
 140 ary satellite data. We follow modern model evaluation standards and sequentially de-
 141 rive synthetic satellite observations using a satellite simulator (similar to Bodas-Salcedo
 142 et al., 2011; Pincus et al., 2012; Matsui et al., 2019) and cloud products with an advanced
 143 cloud classification software. For the latter step, we apply the cloud classification con-
 144 sistentlly for the full diurnal cycle (including nighttime). This improves the attribution
 145 of instantaneous CREs to different cloud types.

146 The paper is organized as follows: In section 2, the setup of the ICON model sim-
 147 ulations and sensitivity studies is described. Sect. 2 also provides information on the ob-
 148 served and synthetic narrow-band satellite radiances that are forwarded into the cloud
 149 classification software and on our method for deriving TOA radiation fluxes from Me-
 150 teosat observations. Sect. 3 presents the main results. We first consider domain-averaged
 151 radiation fluxes and CREs, and then split cloud cover and radiative effects into contri-
 152 butions from different cloud types. A summary and conclusions are given in section 4.
 153 A more detailed description of the modifications of the cloud classification software and
 154 supporting information is provided in the supplement.

155 2 Data and Methods

156 2.1 Overview of the Analyses Workflow

157 Before we provide more details, Fig. 1 presents an overview of the workflow and
 158 analyses steps for observations (black) and simulations (blue). Used acronyms are listed
 159 in Tab. 1. The diagram is to be read from top to bottom. The input data from Meteosat
 160 SEVIRI (see Sect. 2.2) and ICON (see Sect. 2.3) are provided in the first row. From these,
 161 observed and simulated cloud types (Fig. 1a) and CREs (Fig. 1b) are derived, as shown
 162 in the last row. Importantly, this workflow makes sure that observations and simulations
 163 are directly comparable to each other.

164 For cloud classification, ICON simulations are translated into observation space us-
 165 ing the SynSat forward operator (Sect. 2.3). Based on observed and synthetic infrared
 166 BTs, cloud types are derived with the help of the NWCSAF v2013 software (Sect. 2.4).
 167 For the assessment of CREs, Meteosat SEVIRI data are processed to obtain GERB-like
 168 all-sky radiation fluxes at the top of the atmosphere (Sect. 2.2). The observed all-sky
 169 fluxes are supplemented by simulated clear-sky fluxes, which are corrected with a scal-

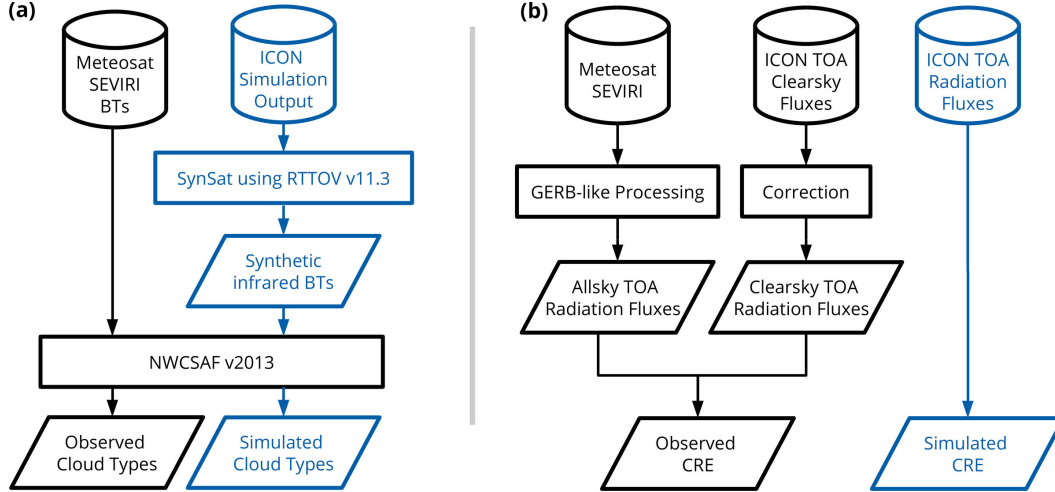


Figure 1. Overview of the workflow for (a) the calculation of a consistent cloud classification and (b) the derivation of CREs. Two parallel paths for observations (black) and the simulations (blue) are shown. The symbols in the top row visualize the input data (either satellite data archive or simulation output). Final data are shown in the last row. Rectangles denote processing methods further discussed in the text, and slanted parallelograms correspond to intermediate and final data.

Table 1. List of most important acronyms.

Acronym	Explanation
BT	Brightness Temperature
CRE	Cloud-Radiative Effect
GERB	Geostationary Earth Radiation Budget
ICON	ICOsahedral Nonhydrostatic
NAWDEX	North Atlantic Waveguide and Downstream impact EXperiment
NWCSAF	Satellite Application Facility in support to NoWCasting and very short range forecasting
RTTOV	Radiative Transfer for Television infrared observation satellite Operational Vertical sounder
RRTM	Rapid Radiation Transfer Model
SEVIRI	Spinning Enhanced Visible and InfraRed Imager
SynSat	synthetic satellite imagery
TOA	Top-Of-the-Atmosphere

170 ing factor in the shortwave and a constant additive offset in the longwave part to cor-
 171 rect for biases in simulated ocean surface properties (Sect. 2.5).

172 2.2 Meteosat Observations

173 Observations are provided by measurements of the imaging radiometer SEVIRI (Spin-
 174 ning Enhanced Visible and InfraRed Imager) on board the geostationary satellites of the
 175 Meteosat Second Generation (MSG) series operated by EUMETSAT (European Organ-
 176 isation for the Exploitation of Meteorological Satellites). We utilize multi-spectral data
 177 from SEVIRI’s operational prime service located at a nominal longitude of zero degrees
 178 and a nadir resolution of $3 \times 3 \text{ km}^2$ (Schmetz et al., 2002). An example of upwelling ther-
 179 mal radiation measured at $10.8 \mu\text{m}$ is provided in Fig. 2 (top row). In the atmospheric

180 window at $10.8 \mu\text{m}$, atmospheric gases are relatively transparent and thermal emission
 181 mainly originates from the Earth surface, from clouds or from a combination of the two
 182 (in case of semi-transparent or fractional clouds). High BTs typically represent clear re-
 183 gions, whereas low temperatures represent emission from high cirrus clouds. In the scene
 184 of Fig. 2, a low-pressure system is located in the Atlantic ocean. Its frontal cloud sys-
 185 tem, seen by the low BTs, extends towards the south and approaches the British Islands.
 186 In the western part of this low-pressure system, cold and rather dry air is advected south-
 187 wards together with marine, low-level clouds that formed within the cold sector.

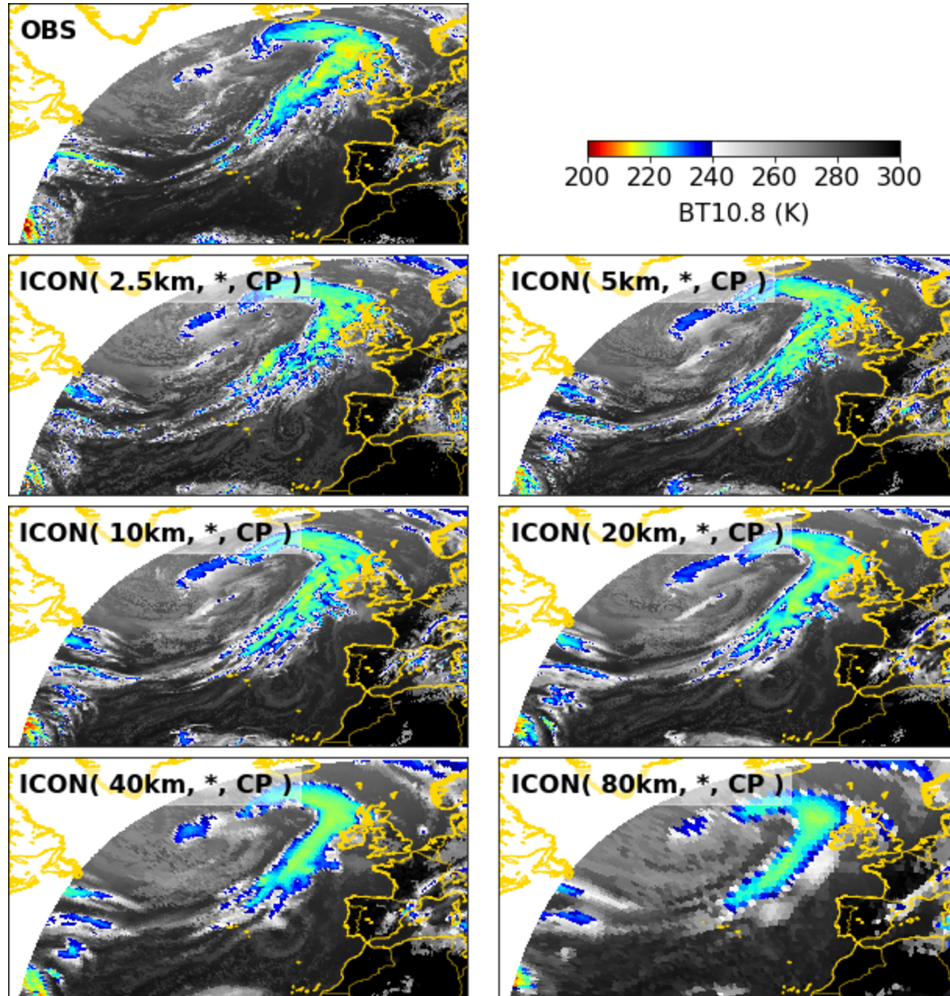


Figure 2. Overview of observed and simulated BTs from Meteosat SEVIRI's window channel at $10.8 \mu\text{m}$ for 1200 UTC 23 Sept 2016. Observations are compared to ICON simulations with increasing grid spacing (left to right and downwards, from 2.5 to 80 km). Only the subset of simulation experiments with one-moment microphysics and fully parameterized convection is chosen for visualization. A special color scheme is used to highlight observed and simulated features. BTs over land are also shown to improve anticipation of the cloud scenery. Further analysis however only considers the Atlantic ocean region.

188 The Meteosat satellites also carry the broadband radiometer GERB (Harries et al.,
 189 2005) for accurate measurements of all-sky TOA radiation fluxes. Unfortunately, dur-
 190 ing the period of our analysis GERB was in "safe mode" to protect its sensors. We there-

191 fore base our TOA radiation flux estimates on SEVIRI data. So-called GERB-like ra-
 192 diation flux products are derived as internal products in the Royal Meteorological In-
 193 stitute of Belgium (RMIB) GERB processing system which have been retrieved from the
 194 RMIB archive for our study. All GERB-like processing steps are explained in detail in
 195 Dewitte et al. (2008) and updates on the calibration of SEVIRI data are given in Meirink
 196 et al. (2013). The accuracy of the applied narrowband-to-broadband conversion is 3.5%
 197 for shortwave fluxes F_{sw} and 0.7% for longwave fluxes F_{lw} (Clerbaux et al., 2005). For
 198 a particular scene type, this error must be considered as a systematic error. For estimates
 199 of downwelling shortwave fluxes, temporal variations in the total solar irradiance are taken
 200 into account as described in Mekaoui and Dewitte (2008). Throughout the paper, we use
 201 a positive-upward convention so that upwelling fluxes are positive and downwelling fluxes
 202 are negative (following G. L. Stephens, 2005).

203 2.3 ICON Simulations

204 We analyze simulations with the ICON model in limited-area setup performed over
 205 a large area of the North Atlantic (model version icon-2.1.00 with bug fixes for two-moment
 206 cloud microphysics). The simulations were already described in Stevens et al. (2020) (see
 207 their Fig. 3) and were performed in support to the NAWDEX field campaign of fall 2016
 208 (Schäfler et al., 2018). The domain extends from 78°W to 40°E in longitudinal direc-
 209 tion, and from 23°N to 80°N in latitudinal direction. ICON is used with the numerical
 210 weather prediction physics package in a setup that largely follows the tropical Atlantic
 211 setup of Klocke et al. (2017). ICON is initialized from the Integrated Forecast System
 212 (IFS) analysis data of the European Center for Medium-Range Weather Forecasts (ECMWF)
 213 at 0 UTC. The lateral boundary data are taken from IFS at 3-hourly resolution. When
 214 available, i.e. at 0 UTC and 12 UTC, IFS analysis data are used. In between 3-hr, 6-
 215 hr and 9-hr IFS forecast data are used. The continually updated analysis and forecast
 216 data ensure that the model stays close to the actual meteorology over the simulation pe-
 217 riod over several days (see below). The IFS data is retrieved at the highest available res-
 218 olution in space (~ 9 km horizontal grid spacing). 11 days are analyzed in total. These
 219 result from 4 simulation sets that each cover a time span of 3 or 4 days, and for which
 220 the first day is disregarded as spin-up. The simulations are listed in Tab. 2.

Table 2. List of days simulated with ICON during the period of the NAWDEX field cam-
 paign in fall 2016. N_{sim} is the number of simulations as a result of testing for the sensitivity with
 respect to horizontal resolution and the treatment of cloud microphysics and convection.

	Simulation period	Analyzed days	N_{sim}
Set 1	Sep 20:0UTC - Sep23:0UTC	Sep 21, 22	14
Set 2	Sep 22:0UTC - Sep26:0UTC	Sep 23, 24, 25	20
Set 3	Sep 29:0UTC - Oct02:0UTC	Sep 30, Oct 01, 02	14
Set 4	Oct 02:0UTC - Oct06:0UTC	Oct 03, 04, 05	14

221 The simulations are performed for six horizontal grid spacings of 80, 40, 20, 10, 5
 222 and 2.5 km. In the vertical, always the same set of 75 levels is used. The thickness of the
 223 lowest model layer above ground is 20 m. The model layer thickness increases to ≈ 100 m
 224 at 1 km altitude above ground up to 1200 m at the model top of 30 km. Sweeping through
 225 the horizontal resolution allows us to cover both the horizontal resolution of present-day
 226 global climate models, which typically run at 50-100 km, as well as the resolution of ex-
 227 isting convection-permitting regional climate simulations (Prein et al., 2015) and upcom-
 228 ing global simulations (Stevens et al., 2019), which run at 2-5 km. Depending on hor-
 229 izontal resolution, subgrid-scale convection is parameterized following Bechtold et al. (2008)
 230 based on the scheme of Tiedtke (1989). When fully enabled, the convection scheme in-

231 tractively decides on the type of convection to be activated, either deep, mid-level or
 232 shallow convection. For the finest resolution of 2.5 km the convection parameterization
 233 scheme is switched off either fully or partly. In the latter setup, only shallow convection
 234 is parameterized, whereas mid-level and deep convection are explicitly represented (ICON
 235 Model Tutorial April 2018). The setup with only shallow convection parameterization
 236 has emerged as the standard setup for 2.5km-ICON simulations at the German Weather
 237 Service (pers. comm. A. Seifert). For resolutions of 5 km and coarser, the convection scheme
 238 is fully enabled and takes care of shallow as well as mid-level and deep convection. In
 239 addition, for a three-day subset (Sep 22, 23, and 24), the 2.5 km simulations are repeated
 240 with fully enabled convection parameterization, and the 5 and 10 km simulations with
 241 fully disabled convection parameterization. This allows us to compare the impact of the
 242 convection scheme with respect to changes in resolution. Besides assessing the impact
 243 of resolution and representing convection in an explicit or parameterized manner, we study
 244 the impact of representing cloud microphysics. To this end, all simulations are performed
 245 with the one-moment cloud microphysical scheme with graupel described in Baldauf et
 246 al. (2011) as well as with the two-moment cloud microphysical scheme of Seifert and Be-
 247 heng (2006). The one-moment scheme is currently used operationally by the German Weather
 248 Service; the two-moment scheme is used in large-eddy mode simulations with ICON (Heinze
 249 et al., 2017).

250 To indicate the model setup in the plots and tables, the following nomenclature is
 251 used. For instance ICON(10km, *, CP) refers to ICON simulations with 10 km grid
 252 spacing, one-moment microphysics and fully enabled convection parameterization. In con-
 253 trast, ICON(2.5km, **) refers to ICON simulations with 2.5 km grid spacing, two-
 254 moment microphysics and fully disabled convection parameterization - a setup that is
 255 called "simulation with explicit convection" in the following. Lastly, ICON(2.5km, **,
 256 sCP) refers to a simulation in which only the shallow convection parameterization is
 257 enabled. Tab. 3 summarizes the model setups.

Table 3. Overview of different treatment of convection for the four sets of simulations (see Tab. 2). sCP means that only the shallow convection scheme is active. CP means that convection is fully parameterized. A notation example is given in the last row for simulations with 2.5 km grid spacing and one-moment cloud microphysics (indicated by *; two-moment cloud microphysics are indicated by **).

	explicit convection	sCP	CP
Set 1, 3, 4	2.5 km	2.5 km	5 - 80 km
Set 2	2.5, 5, 10 km	2.5 km	2.5 - 80 km
Notation example	ICON(2.5km, *)	ICON(2.5km, *, sCP)	ICON(2.5km, *, CP)

258 Radiative transfer is calculated by the global model version of the Rapid Radia-
 259 tion Transfer Model, RRTMG (Mlawer et al., 1997). RRTMG uses a reduced number
 260 of g -points (g is the relative rank of the atmospheric absorption coefficient within a wave
 261 length interval) for the correlated k-method to mitigate some of the computational bur-
 262 den of the parent RRTM model. 14 bands are used in the shortwave, 16 bands are used
 263 in the longwave. The solar constant is set to 1361.4 Wm^{-2} . The diffuse ocean albedo is
 264 set to a constant value, $\alpha_{\text{dif}} = 0.07$. The direct ocean albedo follows the radiation scheme
 265 of Ritter and Geleyn (1992) and is a function of the diffuse albedo and the solar zenith
 266 angle, μ_0 ,

$$267 \alpha_{\text{dir}} = \frac{1 + 0.5 \cos \mu_0 (\alpha_{\text{dif}}^{-1} - 1)}{(1 + \cos \mu_0 (\alpha_{\text{dif}}^{-1} - 1))^2}. \quad (1)$$

268 The maximum value allowed for α_{dir} is 0.999. The diffuse and the direct ocean albedo
 269 are independent of wavelength do not depend on surface roughness and wind speed.
 270 For cloud overlap, the generalized maximum-random overlap scheme of Hogan and Illingworth
 271 (2000) is used, with a vertical decorrelation length scale of 2 km. Ozone is specified
 272 according to the Global and regional Earth system Monitoring using Satellite and
 273 in situ data (GEMS) climatology (Hollingsworth et al., 2008), and aerosol according to
 274 the climatology of Tegen et al. (1997). Only aerosol-radiation-interactions are considered,
 275 aerosol-cloud interactions are not taken into account. The cloud droplet number
 276 used in the radiation for the effective radius of droplets and crystals follows a prescribed
 277 vertical profile taken from the global atmosphere model ECHAM6 (Stevens et al., 2013).
 278 Cloud optical properties, i.e., single scattering albedo, extinction coefficient and asymmetry
 279 factor, are also specified as in ECHAM6. Radiation is called every 12 minutes. The
 280 radiation fields are output every hour and are always consistent with the simulated cloud
 281 field, insolation, solar zenith angle and the state of the atmosphere and surface. Simulated
 282 radiation fluxes were re-gridded onto the observational grid (Sect. 2.2). The analysis
 283 is restricted to ocean areas free from sea ice, which avoids complications from differences
 284 in surface albedo. As such, the analysis domain includes the North Atlantic and
 285 connected water bodies, including the North sea and the Baltic sea (see e.g. Fig. 2 and
 286 Fig. 4). The southern boundary is at 28.3°N and is determined by the boundary nudging
 287 zone of the 80 km grid. A maximum satellite zenith angle of 75° marks the northern
 288 boundary of the domain.

289 For a fair comparison between observations and simulations, the simulated data
 290 have to be transformed into the observational space using forward operators (or sometimes
 291 called instrument simulators). This has become a standard approach in the last
 292 decades (Morcrette, 1991; Roca et al., 1997; Chaboureaud et al., 2000) and is especially
 293 important when such ambiguous variables like cloud cover and cloud types are taken into
 294 consideration (e.g. Pincus et al., 2012). For our study, we apply the so-called SynSat
 295 operator after Keil et al. (2006) and Senf and Deneke (2017) to derive synthetic satellite
 296 images with the sensor characteristics of MSG SEVIRI. The SynSat operator prepares
 297 vertical profiles of atmospheric temperature, humidity, condensate content and subgrid-scale
 298 cloud cover as well as several surface variables to perform single-column radiative
 299 transfer calculations with the RTTOV model (Saunders et al., 1999; Matricardi et al.,
 300 2004), here version 11.3. Radiative transfer calculations are performed for different streams
 301 per vertical column which are combined using the maximum-random overlap assumption.
 302 We apply a standard configuration that has been operationally employed by the
 303 German Weather Service for several years and utilized for ICON simulations in previous
 304 studies (Heinze et al., 2017; Senf et al., 2018; Pscheidt et al., 2019). For this, diagnostic
 305 subgrid-scale cloud condensate content is added to its grid-scale counterpart, and ice
 306 and snow masses are simply combined to a frozen condensate content. Radiative properties
 307 of frozen condensate are estimated using relations for randomly-oriented hexagonal
 308 columns after Fu (1996) and McFarquhar et al. (2003). The derivation of synthetic
 309 BTs is impacted by uncertainties in the formulation of microphysical and radiative
 310 hydrometeor properties. A complicating fact is that different model parameterization
 311 handle hydrometeor properties differently leading to model-internal inconsistencies as
 312 additional cause for uncertainties in the forward calculations. Considering these issues and
 313 typical parameter variations, Senf and Deneke (2017) showed that uncertainties in BTs
 314 are in the order of a few Kelvin and largest for semi-transparent cirrus clouds with low
 315 cloud-top temperatures and with emissivities close to 0.5.

316 Fig. 2 also provides a sequence of synthetic BTs for different model grid spacings
 317 from 2.5 to 80 km. As expected, the simulations capture the general cloud scenery and
 318 the synoptic-scale features very well. All simulations show the frontal cloud band that
 319 approaches the European continent and the upper-level trough located upstream in the
 320 North Atlantic. The coarser the resolution, the less detail can be seen in the synthetic

BT-fields. However, no abrupt quality changes appear to happen with increased grid spacing.

2.4 Cloud Classification

A cloud classification is derived from simulation and satellite data with the NWCSAF software version 2013. As input, the NWCSAF software expects multi-spectral data of MSG SEVIRI in its native data format. Using a set of several multi-spectral tests, a categorical classification is derived for all pixels classified as cloudy (Derrien & Le Gléau, 2005). The applied thresholds mainly depend on the illumination, the viewing geometry, the geographical location and numerical forecast data describing the moisture and thermodynamic structure at coarser resolution. For the latter, short-term IFS forecasts are supplied.

Cloud types are mainly distinguished by their cloud-top height and opacity similar to the ISCCP-approach (International Satellite Cloud Climatology Project, see e.g. Rossow and Schiffer (1999)). No further distinction between convective and stratiform cloud structures is performed. The typical properties of the NWCSAF cloud types are shown in Fig. 3 and contrasted to the categorization after Hartmann et al. (1992). For practical reasons, we consider planetary albedo instead of cloud-optical thickness as measure of cloud opacity. Clouds are divided into different height classes: very low, low, mid-level, high and very high clouds are approximately separated by cloud-top altitudes of 2, 3.5, 6.5 and 9.5 km. These values correspond to pressure levels of 800, 650, 450 and 300 hPa and to environmental temperatures of +8, 0, -18 and -40°C. Therefore, very low and low clouds are purely liquid clouds, mid-level and high cloud categories might contain a mixture of hydrometeor phases, and very high clouds are completely glaciated at cloud top. As shown in Fig. 3, the high and very high clouds are further subdivided by different opacity levels and called: semi-transparent (semi.) thin, semi. moderately thick, semi. thick cirrus as well as high and very high opaque clouds. We call all these categories together "cirrus clouds". The very high opaque clouds might also contain deep convective cores and parts of anvils close to upper-level convective outflow. An additional class is used for fractional clouds for which multi-spectral signatures of clouds and underlying surface are identified. Fractional clouds are typically made of small boundary-layer cumuli. The separation between this and the very-low cloud category is rather artificial. We therefore combine these two classes and end up with eight cloud types that will be utilized for further analysis. No undefined class exists, i.e. satellite pixels are either classified as cloud-free ($k = 0$) or cloudy ($k > 0$). Therefore, the total domain-average cloud cover can be estimated from the sum of fractions of the individual cloud types.

For very low / fractional clouds ($k = 1$ and $k = 9$ in Fig. 3), very low albedo values (close to the clear-sky albedo of ~ 0.1) are most probable. This cloud type mainly consists of shallow clouds with low geometrical and optical thicknesses especially due to high sub-pixel variability and considerable clear-sky contributions. For more opaque clouds with higher cloud tops, averaged albedo shifts to higher values. These cloud types have larger vertical and horizontal extent, and thus higher cloud-optical thicknesses. A similar shift to higher albedo values is found for semi-transparent cirrus going from semi. thin ($k = 6$) to semi. moderately thick ($k = 7$) to semi. thick ($k = 8$). Cloud-spatial structures and sub-pixel variability might be also an important factor for the albedo of semi-transparent cloud categories.

The NWCSAF software has undergone more than a decade of development and is highly adjusted to the needs of operational forecasters and nowcasting applications. It tries to account for as much information as available to derive a comprehensive and instantaneous classification of the cloud field. Changes in solar illumination can lead to changes in product quality and systematic differences, especially between day- and night-

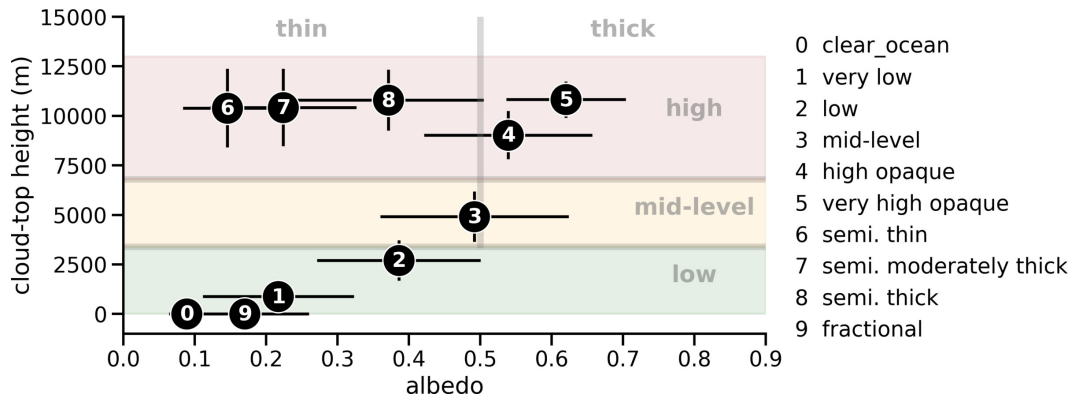


Figure 3. Planetary albedo versus cloud-top height for the different NWCSAF classes. The circles represent averages and the error bars give the standard deviation of clear-sky or cloud properties. Data have been taken from the observed scenery shown in Fig. 2 and 4. Numbers $k = \{0 \dots 9\}$ refer to the different classes listed in the legend. Note that the cloud classes “fractional” and “very low” (which are shown separately here) are combined in the following analysis. For comparison, a second categorization after Hartmann et al. (1992) is provided as background image. It separates cloud amounts into three height categories (low, mid-level and high) as well as into two opacity levels (thin and thick clouds).

372 time, are inevitable in the standard setup of the NWCSAF cloud classification. To mit-
 373 igate these problems and to build a time-consistent cloud classification, we implemented
 374 a modification to the cloud product generation chain. The NWCSAF software has been
 375 set up to run in permanent-night conditions at which only infrared radiation of terres-
 376 trial origin is utilized. We developed an algorithm which reads in infrared SEVIRI ra-
 377 diances from a selected scene and thereafter outputs these data into a template valid for
 378 the same day, but for 0 UTC. The template files, including the embedded satellite ra-
 379 diances, are supplied to the NWCSAF software which generates a cloud classification in
 380 night-mode. To keep the software itself unmodified, we provide simple estimates of ra-
 381 diances at $3.9 \mu\text{m}$ which are mandatory, but contaminated with sunlight during day-time
 382 (further explained in the supplement). Beyond time consistency, there is an other ma-
 383 jor advantage of our approach: It also allows to exchange real observations with synthetic
 384 observations. In our case, we utilized synthetic radiances derived from all the different
 385 simulations with the SynSat method (see Sect. 2.3) and provide these data to the NWC-
 386 SAF software. In this way, a cloud classification is obtained for all simulations that is
 387 directly comparable to its observational counterpart.

388 An example scenery of an instantaneous and high-resolution cloud classification is
 389 shown in Fig. 4. The scene is similar to the one shown in Fig. 2, but here the focus is
 390 on 2.5 km simulations with different treatment of convection and cloud microphysics. A
 391 frontal cloud band extends from the British Island to the open Atlantic. West of this cold
 392 front, marine clouds of type “low” and “very low / fractional” propagate towards the
 393 European continent. In the subtropical areas, Meteosat observations show a rather low
 394 fraction of low and very low / fractional marine clouds. The amount of these cloud types,
 395 which appear in large patches of marine stratocumulus, is strongly overestimated. This
 396 is a common bias in all considered ICON simulations at 2.5 km, especially in the vari-
 397 ants with explicit convection (see also (Senf et al., 2018)), and might reflect weaknesses
 398 in the setting and coupling of the convection scheme and planetary-boundary layer scheme.

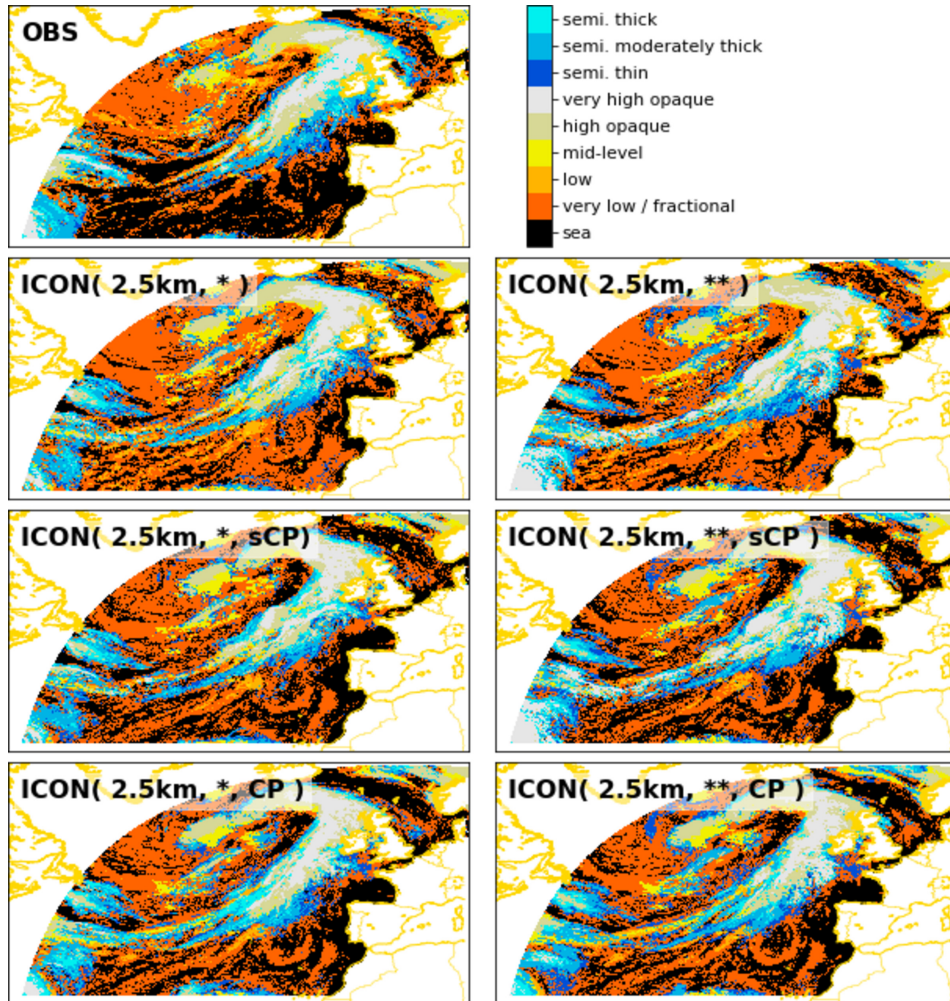


Figure 4. Example of observed and simulated cloud types for 1200 UTC 23 Sept 2016 as derived from Meteosat SEVIRI observations (top left) and ICON simulations with 2.5 km horizontal resolution. The left column is for simulations with one-moment cloud microphysics (*), the right column for simulations with two-moment microphysics (**). The second row is for fully explicit convection, the third row for simulations with a shallow convection scheme (sCP), and the fourth row for simulations with fully parameterized convection (CP).

399

2.5 Estimation of Observed Clear-Sky Radiation Fluxes

We are interested in the cloud impact on broadband shortwave and longwave radiation fluxes. This impact is commonly measured in terms of cloud-radiative effects (CREs),

$$\text{CRE}_{\text{net}} = \overline{F_{\text{net,clear}}} - \overline{F_{\text{net}}}, \quad (2)$$

400 which are defined as time-average difference between hypothetical clear-sky fluxes that
 401 would occur in the absence of clouds and cloud-affected all-sky fluxes. We follow the sign
 402 convention of G. L. Stephens (2005) and remind the reader that we defined upwelling
 403 all-sky and clear-sky fluxes as positive. Positive CREs indicate a gain of radiative en-
 404 ergy and a warming effect of clouds, negative CREs indicate a loss of radiative en-
 405 ergy and a cooling effect. Note that CREs are the net result of different cloud types; the ra-
 406 diative impact of individual cloud types is analyzed later in Sect. 3.2.

407 The ICON simulations provide all-sky and clear-sky fluxes, where the latter are cal-
 408 culated via a second radiation call with cloud fields set to zero. Simulated CREs follow
 409 directly from the application of eq. (2). Deriving clear-sky fluxes for the observations is
 410 more difficult. Observational clear-sky fluxes could be estimate from all-sky fluxes in re-
 411 gions classified as cloud-free, but these might contain undetected clouds and could be
 412 biased toward drier and more stable atmospheric conditions (Sohn et al., 2010). For our
 413 analysis the situation is even more challenging because (i) the North Atlantic is very cloudy,
 414 and (ii) we are interested in instantaneous high-resolution radiation fluxes and CREs,
 415 for which the clear-sky fluxes cannot be derived by temporal and spatial aggregation (as
 416 done in, e.g., Futyán and Russell (2005)). We therefore apply the following recipe to es-
 417 timate observational clear-sky fluxes (clear-sky path in Fig. 1b):

- 418 (i) Clear-sky fluxes are taken from simulations as first guess (similar to Allan, 2011).
 419 The ICON(10km, *, CP) experiment has been chosen as reference.
- 420 (ii) A bias correction is applied to simulated clear-sky fluxes under the constraint that
 421 the *radiative effects of undetected clouds have similar magnitudes in observations*
 422 *and simulations.*

423 The second step is based on the fact that for ICON simulations, differences between
 424 clear-sky and all-sky radiation fluxes are also available for regions that are classified as
 425 cloud-free ($k = 0$). As shown in Fig. 5, these differences are not zero and are caused
 426 by undetected clouds. We thus need to distinguish between all-sky and clear-sky fluxes
 427 in cloud-free regions. Therefore, a distinction between “cloud-free” and “clear-sky” is
 428 made throughout the rest of the paper.

429 The radiative effects of undetected clouds help us to establish a bias correction to
 430 translate simulated clear-sky fluxes into observational estimates (see also supplement)
 431 and to assess the quality of the NWCSAF cloud detection (modified by us to run in night-
 432 mode). For a perfect cloud classification, all values should be at zero. This is not the case,
 433 however, and this demonstrates that a small amount of clouds remains undetected. Un-
 434 detected clouds from the simulations contribute around 3 W m^{-2} of additional shortwave
 435 reflection in cloud-free regions (Fig. 5a). In the longwave, simulated flux differences are
 436 between 1 and 2 W m^{-2} in cloud-free regions (Fig. 5b) and result from the reduced emis-
 437 sion temperature of undetected clouds. The shortwave and longwave effects of undetected
 438 clouds partially cancel. When weighted by the fraction of cloud-free areas of around 25%,
 439 we conclude that CREs of undetected clouds have negligible impact on the total domain-
 440 average radiation budget.

441 Fig. 5 additionally shows two observational estimates of the effects of undetected
 442 clouds: one just takes uncorrected (first-guess) ICON clear-sky fluxes (gray symbols) and
 443 the other one uses bias-corrected ICON clear-sky fluxes (black symbols). It can be seen
 444 that the bias correction brings the observational estimates close to the simulations. The
 445 bias correction reduces the first-guess clear-sky fluxes by 4 to 6 W m^{-2} in the shortwave
 446 and by 2 W m^{-2} in the longwave. We believe the overestimation in the shortwave results
 447 from a too bright ocean surface albedo in ICON. Additional support for this interpre-
 448 tation comes from independent internal investigations by the German Weather Service
 449 (pers. comm. A. Seifert). Moreover, simulated ocean surface seems to be too warm caus-
 450 ing an overestimation of outgoing longwave clear-sky fluxes that adds to the shortwave
 451 bias.

452 Technically, an offset of 2 W m^{-2} is subtracted from $F_{\text{lw,clear}}$ as simple bias cor-
 453 rection in the longwave. For the shortwave, it is more appropriate to apply a scaling fac-
 454 tor to the upwelling flux $F_{\text{sw,up,clear}}$ (see Fig. 6). A scaling factor of 0.88 brings the ICON
 455 curve approximately down to the observational curve. Fig. 6 also shows that all ICON
 456 simulations lie together closely. It is therefore of minor importance which ICON exper-
 457 iment is chosen as reference. After correction, the simulated clear-sky fluxes are used to-

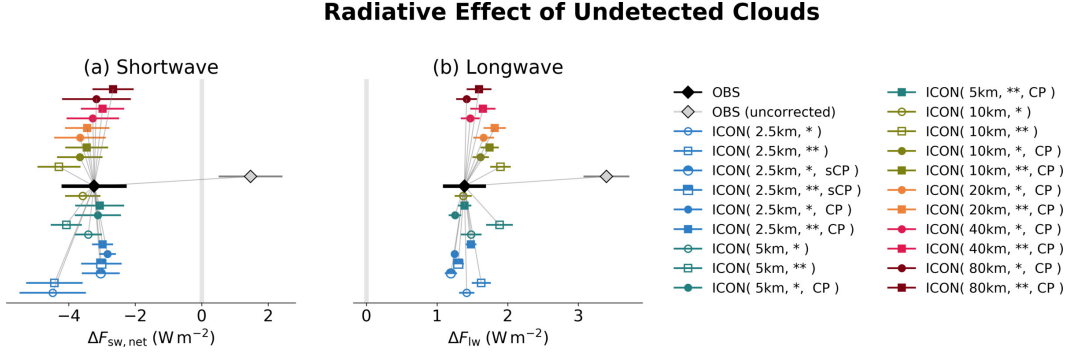


Figure 5. The radiative effect of undetected clouds in areas classified as cloud-free (i.e. $k = 0$). All data points show the average difference between clear-sky and all-sky fluxes for (a) shortwave $\Delta F_{sw,net} = F_{sw,net,clear} - F_{sw,net}$ and (b) longwave $\Delta F_{lw} = F_{lw,clear} - F_{lw}$. The bars give an robust estimate of the standard error of the daily-average values over all simulation sets, thus provide a confidence interval. For this, the difference between the 84-th and 16-th percentile has been calculated to approximate twice the multi-day standard deviation 2σ which was further divided by \sqrt{N} with $N = 11$ for the all experiments except the additional runs from simulation set 2 (see Tab. 3). Colored symbols represent different simulations which have been vertically stacked to improve visibility. The gray symbols show the uncorrected observational estimate where the all-sky fluxes are based on Meteosat, but the clear-sky fluxes are directly taken from ICON(10km, *, CP). The black symbols show the corrected observational values with a scale factor applied to the shortwave and a constant additive offset to the longwave part of clear-sky fluxes taken from ICON(10km, *, CP). Thin gray lines connect all other symbols to the observation for improved interpretation. The clear-sky bias of the simulations is directly obtained from the difference between black and gray symbols.

458 together with observed all-sky fluxes for the calculation of observed CREs using eq. (2).
 459 In summary, the applied strategy for cloud classification is extremely helpful to estab-
 460 lish a consistent bias correction of instantaneous clear-sky fluxes estimated from simu-
 461 lations.

462 3 Results

463 3.1 Domain and Time-Averaged Radiation Fluxes and Cloud-Radiative 464 Effects

465 We begin with a comparison of observed and simulated radiation fluxes averaged
 466 over the North Atlantic domain and all days (Fig. 7). The observed net flux is around
 467 25 W m^{-2} and directed outward (Fig. 7a), implying that in this time of the year the North
 468 Atlantic region loses more radiative energy than it gains. All simulations show larger
 469 net fluxes, indicating that they overestimate the loss of radiative energy. Simulations with
 470 partly or fully parameterized convection have a net flux of around 30 W m^{-2} , with the
 471 coarsest resolution showing the smallest deviation with respect to observations. Further-
 472 more, simulations with fully parameterized convection have net fluxes slightly closer to
 473 the observation when using one-moment microphysics instead of two-moment microphysics.
 474 This might reflect previous model tuning that was done for one-moment but not for two-
 475 moment microphysics. Simulations with parameterized shallow convection show net fluxes
 476 very similar to simulations with fully parameterized convection. Much stronger devia-
 477 tions occur, however, for simulations with explicit convection, for which the net flux reaches

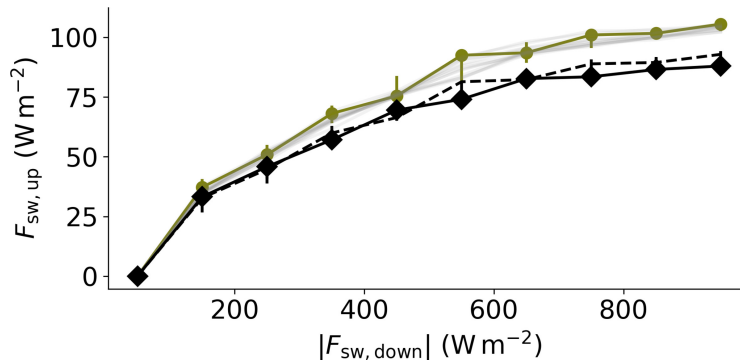


Figure 6. Simulated and observed upwelling versus downwelling shortwave fluxes in cloud-free areas. The upwelling flux is calculated for 10 bins of the downwelling flux. Symbols denote conditional median values and error bars show the inter-quartile range. Simulations are shown in gray, with the simulations for ICON(10km, *, CP) shown in olive green. Observations are shown by the black diamonds and the black solid line. The dashed black line shows the upwelling flux from ICON(10km, *, CP) rescaled by a factor of 0.88.

478 about 40 W m^{-2} . We note that the deviations in the net flux are not simply a result of
 479 differences in the downwelling shortwave flux, which amount to 1 W m^{-2} due to slight
 480 differences in the solar constant in the simulations and observations.

481 The better agreement in terms of the net flux for low-resolution simulations and
 482 for simulations with (partly) parameterized convection results from compensating biases
 483 in outgoing longwave fluxes and upwelling shortwave fluxes (Fig. 7b and d). These compensating
 484 radiation flux biases are a known problem of a large number of climate models where tuning was aimed in particular at the net TOA energy balance (Klein et al.,
 485 2013). With one exception, the simulations overestimate outgoing longwave radiation
 486 (Fig. 7b), which corresponds to a too high effective emission temperature. The longwave
 487 bias increases with increasing grid spacing, with the largest bias found for the coarsest
 488 simulation at 80 km resolution. Simulations with fully parameterized convection underestimate
 489 upwelling shortwave radiation, which corresponds to a too low planetary albedo.
 490 Similar to the longwave bias, the shortwave bias is stronger for the coarser simulations.
 491 The better agreement in the net flux found for the coarser simulations is thus achieved
 492 for the wrong reason: a systematic bias compensation between longwave and shortwave
 493 fluxes that increases when a coarser resolution is used. Put differently, this also means
 494 that bias compensation becomes smaller as the resolution is made finer - an encouraging
 495 signature of convergence with increasing resolution. Similarly, Hohenegger et al. (2020)
 496 found that net shortwave TOA radiation shows a continuous improvement for successive
 497 grid refinements in their global ICON simulations with explicit convection.
 498

499 For the highest resolution simulations at 2.5 km the outgoing longwave flux improves
 500 when the shallow-convection scheme is disabled so that convection becomes fully explicit.
 501 This is in particular the case for two-moment microphysics, which agrees best with observations
 502 in terms of the longwave flux (Fig. 7b). However, the simulations with fully explicit convection
 503 strongly overestimate the upwelling shortwave flux. As a result, the overall most satisfying
 504 agreement is found for simulations that combine two-moment microphysics and parameterized
 505 shallow convection. The shallow-convection parameterization avoids the strong overestimation
 506 of upwelling shortwave flux found for fully explicit convection.
 507

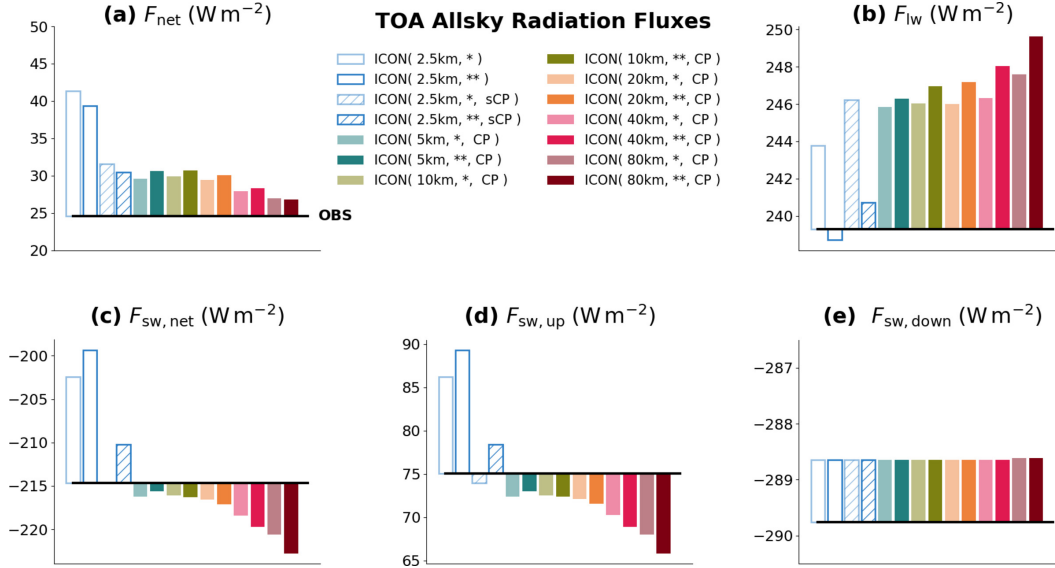


Figure 7. Domain and time-averaged all-sky radiation fluxes: (a) total net flux, (b) outgoing longwave flux, (c) net shortwave flux, (d) upwelling shortwave flux, and (e) downwelling shortwave flux. Observations are shown by the black horizontal lines. The deviations of simulated fluxes with respect to observations are shown by colored bars.

508 The simulation of domain- and time-averaged CREs and cloud cover is analyzed
 509 in Fig. 8. For the observations, CREs are around -41 W m^{-2} in the shortwave and around
 510 27 W m^{-2} in the longwave, with a net cooling effect of clouds of -14 W m^{-2} . These CRE
 511 values are in the same range as global and long-term averaged observations. However,
 512 in the seasonal mean, twice as large CRE values would be found for the North Atlantic
 513 region (Zelinka et al., 2017). Simulated shortwave and longwave CREs are negatively cor-
 514 related, with more positive longwave CREs obtained for more negative shortwave CREs
 515 (Fig. 8a). Simulations with fully parameterized convection lie in the upper left quadrant
 516 of Fig. 8a and thus underestimate the magnitude of both longwave and shortwave CREs.
 517 Although these simulations show some improvement with decreasing grid spacing, none
 518 of the simulations approaches the observed CREs, and the impact of resolution appears
 519 to saturate at grid spacings between 10 and 20 km. This indicates that even if the grid
 520 spacing was further reduced, the simulations would be unable to approach the observa-
 521 tions if convection is fully parameterized. This idea is supported by Fig. S5 (supplemen-
 522 tary material).

523 In contrast, simulations with shallow-convection scheme or with fully explicit con-
 524 vection are scattered around the observations (Fig. 8a). In these simulations, the impact
 525 of grid-scale cloud microphysics is also much more pronounced. This is because less or
 526 no subgrid-scale cloud condensate is produced by the convection parameterization, which
 527 has its own and much simpler convection microphysics description. Overall, this suggests
 528 a clear benefit from (partly) disabling the convection scheme. In fact, simulations with
 529 shallow-convection scheme and two-moment microphysics show a remarkable match with
 530 observed longwave and shortwave CREs.

531 Fig. 8b-d further shows the relation between CREs and cloud cover. In the observa-
 532 tions, cloud cover is around 73%. Cloud cover is a primary control on CREs (e.g. Dolinar
 533 et al., 2015). Unsurprisingly this is visible in the simulations, which show a near-linear
 534 relation between cloud cover and the CREs. In part, this clear relation is due to the fact
 535 that the analyses were only made for one particular model, the ICON model. Greater

536 spread would be expected for the comparison of several models with different paramete-
 537 rizations (see Nam et al., 2012). For our analysis, the observations do not fall onto the
 538 simulation-based relationship. This leads to a dilemma: For none of the simulations do
 539 CREs and cloud cover at the same time match the observations. Cloud cover is better
 540 simulated for coarser grid spacings, whereas CREs improve as the grid spacing is refined.
 541 This indicates that the distribution of cloud-optical thicknesses and, associated with this,
 542 the vertical cloud structure is insufficiently represented in ICON.

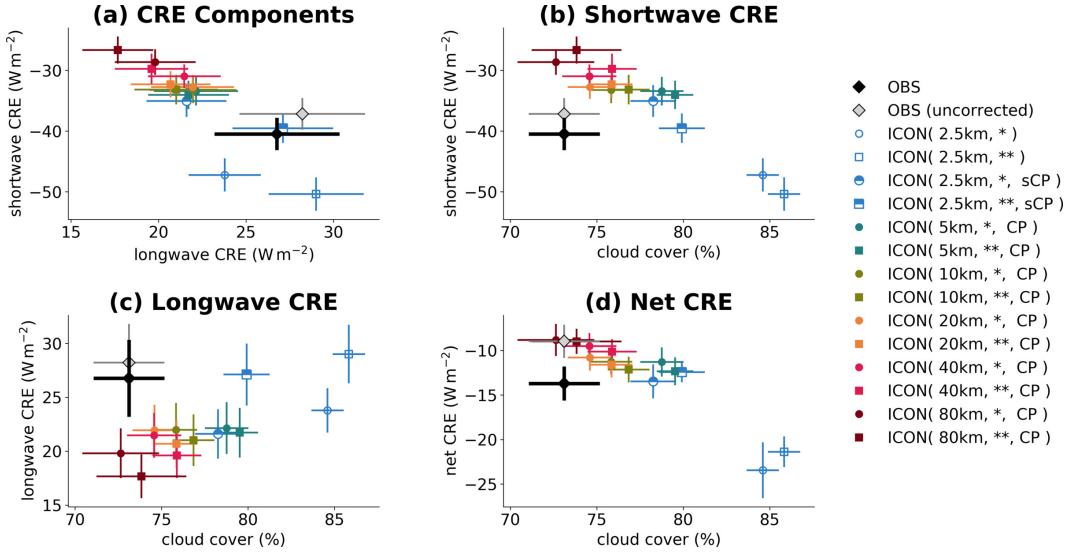


Figure 8. Comparison of domain- and time-averaged cloud-radiative effects and cloud cover: (a) longwave CRE vs. shortwave CRE. Cloud cover vs. (b) shortwave CRE, (c) longwave CRE, and (d) net CRE. Similar to Fig. 5, symbols denote average values and error bars provide confidence intervals. Please note the differences in the y-axis range.

Using Eq. (2) the radiation flux biases of the ICON simulations with respect to observations can be written as the sum of clear-sky and CRE biases, i.e.,

$$\delta\bar{F} = \overline{F_{\text{ICON}}} - \overline{F_{\text{OBS}}} = \delta\overline{F_{\text{clear}}} - \delta\text{CRE}. \quad (3)$$

543 The results of this decomposition are collected in Fig. 9, with net flux biases shown in
 544 the left column, shortwave flux biases in the middle column, and longwave flux biases
 545 in the right column. The matrix presentation of Fig. 9 allows for two implicit summing
 546 rules: the left column is the sum of the middle and right columns, and the first row is
 547 the sum of 2nd and 3rd rows. The second row of Fig. 9 shows that net biases are to a
 548 substantial extent due to clear-sky biases, which are independent of the simulation setup
 549 and amount to $\sim 7.4 \text{ W m}^{-2}$. The biases in simulated clear-sky fluxes have already been
 550 identified in Sect. 2.5 where a correction for observational clear-sky estimates was con-
 551 structed. The clear-sky bias mostly arises from the shortwave ($\sim 5.6 \text{ W m}^{-2}$), with a
 552 smaller longwave contribution ($\sim 1.8 \text{ W m}^{-2}$). The magnitude of the clear-sky short-
 553 wave bias is somewhat surprising, and likely reflects an imperfect representation of ocean
 554 surface albedo in the ICON simulations.

555 The dependence of all-sky flux biases on resolution and the treatment of convec-
 556 tion and cloud microphysics results entirely from CREs (Fig. 9, third row). The net CRE
 557 bias counteracts the clear-sky bias and thus reduces the net all-sky bias for simulations
 558 with fully parameterized convection. For simulations with fully explicit convection, the
 559 net CRE bias adds to the clear-sky bias and therefore increases the net all-sky radiation

560 bias. For simulations with parameterized shallow convection, the CRE biases depend on
 561 cloud microphysics. With one-moment microphysics, the CRE biases are similar to the
 562 biases found for fully parameterized convection. In contrast, with two-moment micro-
 563 physics there is essentially no CRE bias, neither in the shortwave, longwave or net. The
 564 net flux bias of the two-moment simulation with parameterized shallow convection is there-
 565 fore entirely due to clear-sky biases, which could be decreased by adjusting the ocean
 566 albedo.

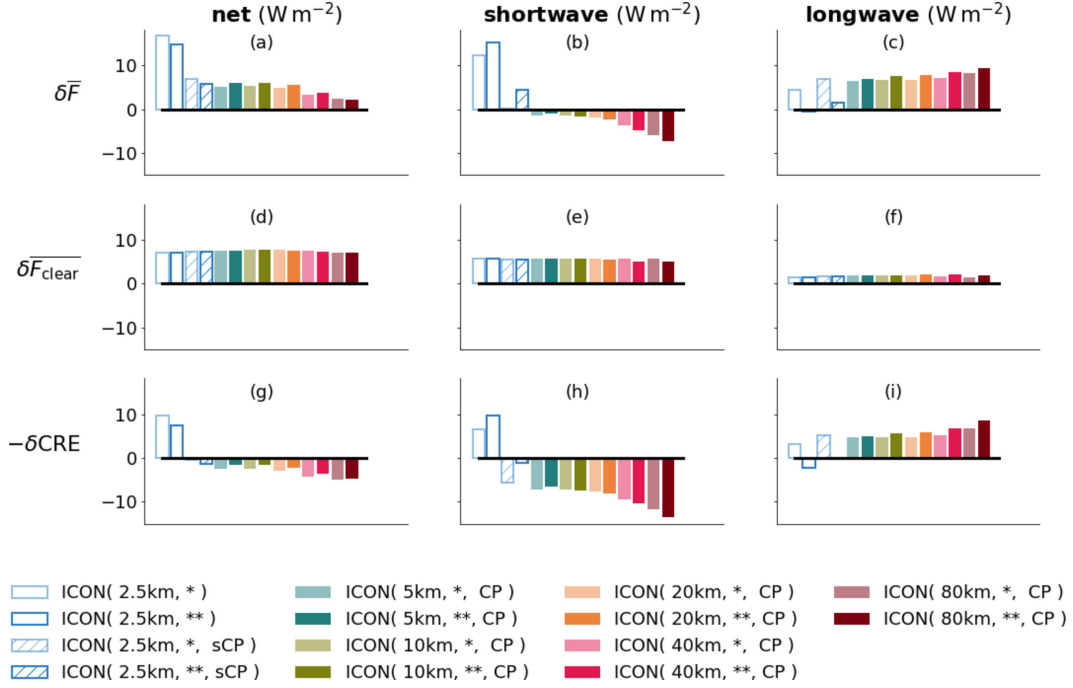


Figure 9. Decomposition of domain- and time-averaged biases for net (left), shortwave (middle) and outgoing longwave (right) radiation fluxes. The all-sky bias (1st row) is the sum of clear-sky (2nd row) and CRE (3rd row) biases. The clear-sky biases are calculated with respect to the bias-corrected clear-sky fluxes of `ICON(10km, *, CP)`, which serves as observational reference.

567 The above analyses have already shown that CRE biases become smaller when the
 568 spatial resolution of ICON is refined. This effect is quantified more precisely in Fig. 10
 569 which shows the resulting CRE biases and their changes for simulation set 2 (see Tab. 3).
 570 For set 2, additional simulations are available, which allow to assess the effect of grid re-
 571 finement on CRE biases simulated with explicit convection. The magnitudes of short-
 572 wave CRE biases become larger for increasing grid spacing from 2.5 to 10 km and ex-
 573 plicit convection (Fig. 10a). The sign of the longwave CRE bias depends on the choice
 574 of the microphysics scheme. For a detailed assessment of the resolution impact, simu-
 575 lation pairs were formed in which one simulation has half the grid spacing of the other
 576 simulation. Microphysics and convection parameterization were chosen identically. Ab-
 577 solute values of the CRE biases were subtracted from each other in such a way that a
 578 positive value indicates an improvement by grid refinement. It can be seen that refin-
 579 ing resolution always improves shortwave CRE biases (Fig. 10c). The improvement is
 580 less pronounced for grid spacings less than 20 km and fully parameterized convection.
 581 This saturation can be overcome when fully explicit convection is used for which refine-
 582 ment down to 2.5 km provides substantial reduction of shortwave CRE biases. For the
 583 longwave, the behavior is different (Fig. 10d). Simulations with fully parameterized con-

584 vection and two-moment microphysics experience continuous improvement with each
 585 refinement step down to 2.5 km. In contrast, longwave CRE biases simulated with explicit
 586 convection and one-moment microphysics even become worse when horizontal resolution
 587 is refined. As a further analysis, simulation pairs were formed which have the same res-
 588 olution and convection parameters, but differ in terms of microphysics. Positive changes
 589 in CRE biases indicate improvements when switching to two-moment microphysics (Fig. 10e
 590 and f). For coarse resolutions, switching to two-moment microphysics leads to worse CRE
 591 biases in the longwave and in the shortwave. For smaller grid spacing and partly or fully
 592 parameterized convection, the sign changes and switching to two-moment microphysics
 593 can now lead to substantial improvements. For simulations with fully explicit convec-
 594 tion, these improvement of CRE biases are only found in the longwave whereas switch-
 595 ing microphysics causes unexpectedly increased biases in the shortwave. The clarifica-
 596 tion of the exact causes for the parameter dependencies found here requires further in-
 597 vestigations.

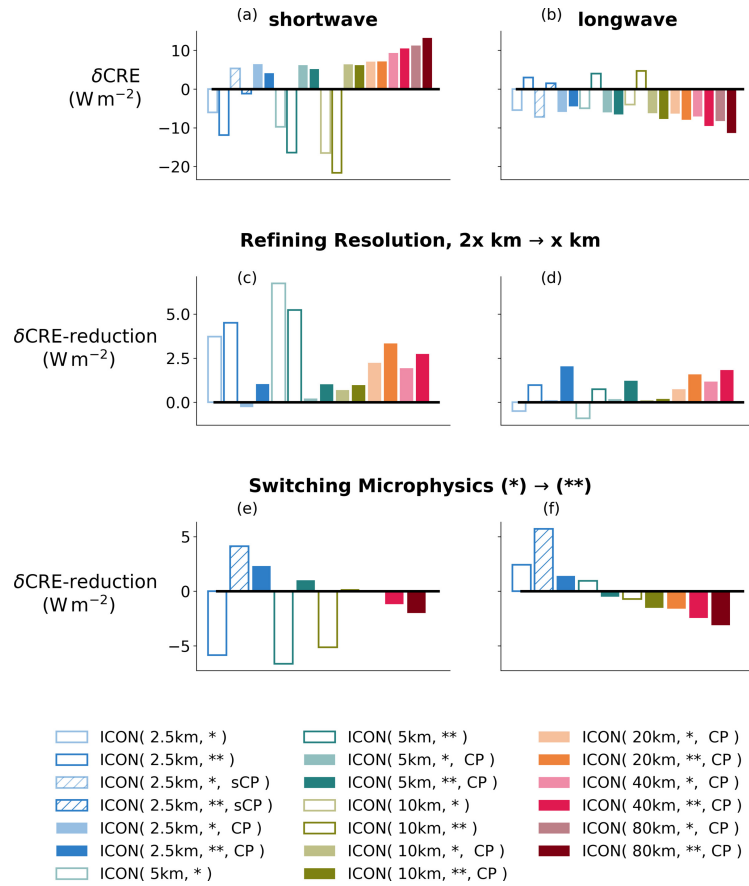


Figure 10. Impact of resolution and microphysics on CRE biases. Similar to Fig. 9h-i, CRE biases are shown for shortwave (left) and longwave (right), but only for simulation set 2 (see Tab. 3). Additionally, it is shown how CRE biases are reduced when resolution is refined (middle row) and microphysics is switched from the one-moment scheme to the two-moment scheme (bottom row). All other parameters were set equal and the ICON experiment, to which it is switched, is indicated in colored bars. A reduction of the CRE bias is shown with positive and increase with negative values.

598
599

3.2 Dependence of Cloud-Radiative Effects and Cloud Cover on Cloud Type

We now explore the origins of the domain- and time-averaged cloud-cover and CRE biases in the ICON simulations. To this end we use the cloud classification outlined in Sect. 2.4, which allows us to quantify the biases as a function of cloud type. This is done by writing the instantaneous domain-averaged net flux, F_{net} , as a sum of contributions from the K cloud types of the cloud classification,

$$F_{\text{net}} = \sum_{k=0}^K f_k F_{\text{net},k}, \quad (4)$$

where f_k is the fractional cloud cover of a certain cloud type k and $F_{\text{net},k}$ is the instantaneous net flux averaged over the area covered by cloud type k . Areas classified as cloud-free are included at $k = 0$. As before a positive sign is taken for upwelling fluxes. Instantaneous domain- and time-averaged CREs are decomposed analogously,

$$\text{CRE}_{\text{net}} = - \sum_{k=0}^K \frac{f_k (F_{\text{net},k} - F_{\text{net,clear},k})}{F_{\text{net},k}}, \quad (5)$$

600
601
602
603

where the cloud type-separated instantaneous net fluxes are averaged over time. This yields to a CRE decomposition into contributions from different cloud types. Note that clear-sky and cloud-free fluxes are not equal, $F_{\text{net},0} \neq F_{\text{net,clear},0}$, because of clouds that are undetected by the cloud classification (cf. Fig. 5).

604
605
606
607
608
609
610

Fig. 11 presents the cloud-type separation of total cloud cover. In the observations, cloud cover is dominated by very low / fractional clouds, which contribute around 30% to the total observed cloud cover of 73%. The three cloud types "low", "high opaque" and "semi. moderately thick" clouds each provide around 10%. The remaining cloud types are less important. From a qualitative point of view, all simulations capture the cloud cover of the different cloud types rather well. A few features of simulated cloud types, however, stand out:

611
612
613
614
615
616
617
618
619
620
621
622
623
624
625
626
627
628
629

- (i) The cloud cover of very low / fractional clouds strongly depends on resolution and is better simulated in coarse-resolution simulations with grid spacings between 10 and 80 km. Finer-resolution simulations substantially overestimate very low / fractional cloud cover, with a more severe overestimation as the grid spacing is decreased. The largest overestimation is found for simulations with shallow or fully explicit convection.
- (ii) Most simulations underestimate the low cloud cover and overestimate the cloud cover of semi-transparent clouds. These biases are less resolution dependent and become smaller when convection is fully explicit.
- (iii) The choice of the microphysics scheme (one-moment vs. two-moment scheme) has a dominant impact on the cloud cover of cirrus clouds, which are represented by the five cloud types "high" and "very high opaque" as well as "semi. thin", "semi. moderately thick" and "semi. thick". The effect is evident for high and very high opaque clouds, for which the two-moment scheme produces smaller cloud cover than the one-moment scheme for fully parameterized convection but higher cloud cover for very high opaque clouds and parameterized shallow convection. At the same time, the two-moment scheme leads to increased cloud cover and cloud-cover biases for semi. thin and moderately thick clouds independent of the treatment of convection.

630
631
632

An overestimation of marine shallow cloud cover has already been observed in Senf et al. (2018), where ICON simulations were performed at 2.5 km grid spacing and with fully explicit convection. This persistent bias can also be found here and is a problem

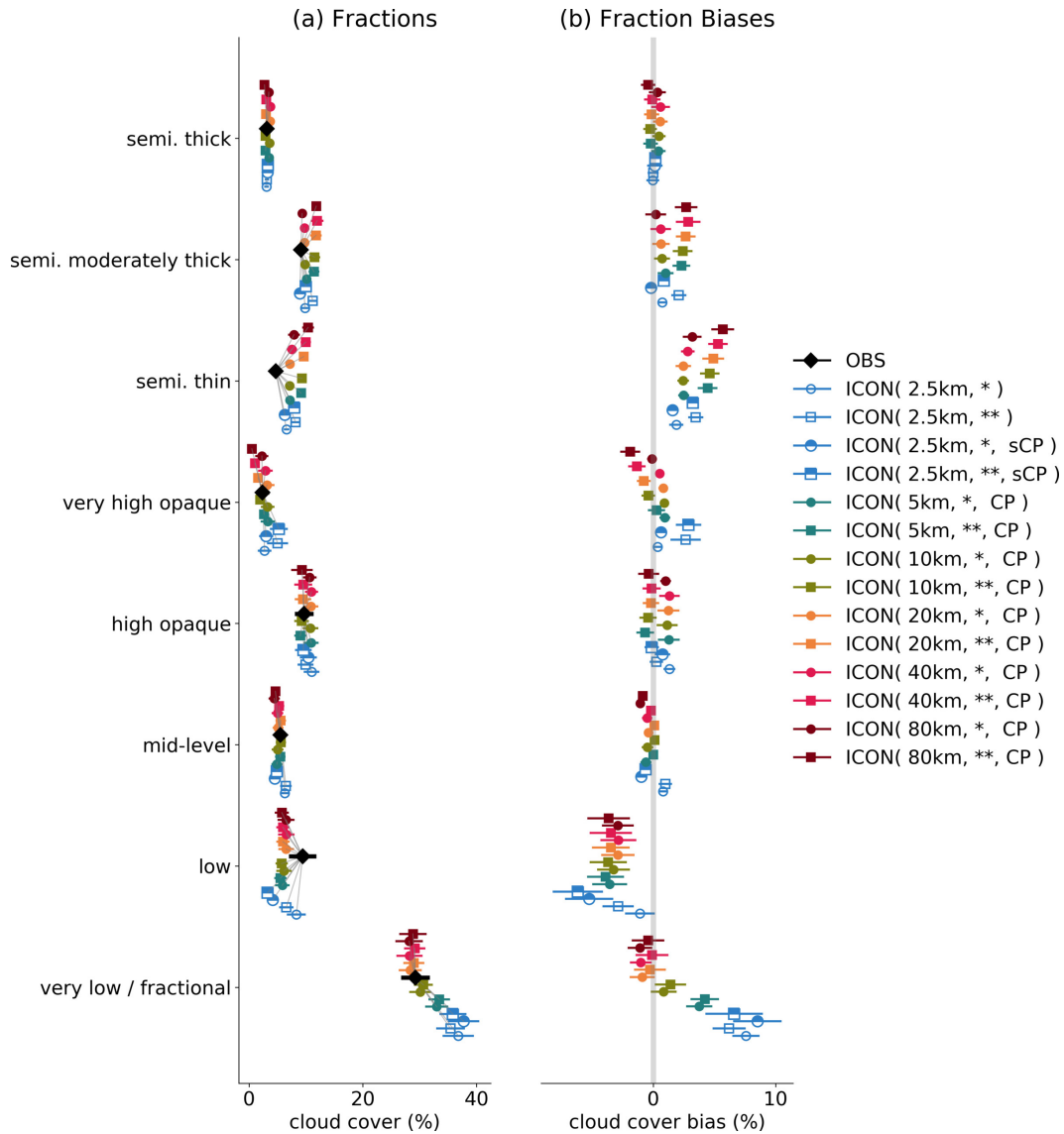


Figure 11. Observed and simulated cloud cover as a function of cloud type (a) as well as cloud cover biases of the simulations with respect to Meteosat observations (b). Similar to Fig. 5, symbols denote average values and error bars provide confidence intervals.

633 especially for simulated cloud coverage in the subtropical regions (see Fig. 4). A grid spac-
 634 ing of 2.5 km is still too coarse, so that the cloud-scale circulations are not sufficiently
 635 resolved. As result, too large and too regular structures of marine stratocumulus appear
 636 in the simulations.

637 To understand the microphysical sensitivity of the simulated cirrus clouds, it must
 638 be considered that the microphysics scheme in ICON was inherited from the weather model
 639 of the Consortium for Small-scale Modeling (COSMO). For COSMO a systematic over-
 640 estimation of the cirrus cover was found (Böhme et al., 2011; Senf & Deneke, 2017). In
 641 order to eliminate this error, adjustments were made in the description of ice microphysics
 642 which reduce the optical thickness of cirrus clouds (Eikenberg et al., 2015; Köhler & Seifert,
 643 2015). In the ICON simulations presented here, this may lead to a situation where semi-
 644 transparent cirrus is more overestimated by the two-moment scheme.

645 The domain- and time-averaged shortwave CRE depends on the typical albedo of
 646 a certain cloud type (see Fig. 3). This relation is further illustrated by Fig. 12a where
 647 CREs have been calculated for a hypothetical overcast situation in which the radiative
 648 effect of each cloud type was considered separately assuming a total coverage of 100%.
 649 Based on observations, very low / fractional clouds induce a rather low shortwave over-
 650 cast CRE of -30 W m^{-2} . The shortwave overcast CRE increases reaching -140 W m^{-2}
 651 for very high, opaque clouds. The concurrent increase of albedo and cloud-top height also
 652 leads to increases in longwave overcast CREs. The imperfect compensation between short-
 653 and longwave CREs causes net effects that have different signs for observed opaque and
 654 observed semi-transparent cirrus clouds. All opaque clouds induce a net cooling due to
 655 their negative net CREs in the observation. For observed low and mid-level clouds, the
 656 magnitudes of net overcast CREs are largest with -50 W m^{-2} . The warming effect of
 657 observed semi-transparent clouds is less pronounced and is largest for semi. thick clouds
 658 with 15 W m^{-2} . These numbers are consistent with the findings of Chen et al. (2000)
 659 who attribute the largest negative shortwave CRE to their deep convective cloud type
 660 (comparable with our opaque very high category) and who also find a positive net CRE
 661 for their cirrus cloud type (comparable to our semi-transparent thin category).

662 The comparison of observed overcast CREs with their simulated counterparts helps
 663 to assess how good the different simulation setups represent the individual cloud-type
 664 specific radiation fluxes (independently of the fractional cloud cover of each type). On
 665 a qualitative level, all simulations perform very well showing the observed dependence
 666 of overcast CREs on cloud type. Most remarkably, none of the simulated semi-transparent
 667 cloud types causes significant positive net CREs (except for ICON(2.5 km, **, sCP)),
 668 i.e. hardly any of the ICON simulations induce a net domain-average warming from semi-
 669 transparent cirrus (see Fig. 12b). For all simulated semi-transparent cirrus cloud types,
 670 the longwave CREs and thus their thermal cloud emissivities are underestimated (see
 671 Fig. 12a).

672 The dependence of all-sky CREs on cloud type is presented in Fig. 12c-d. Follow-
 673 ing eq. (5), all-sky CREs are calculated by weighting the difference between overcast and
 674 clear-sky radiation fluxes by the cloud cover of each cloud type. The relative amount of
 675 each cloud type determines the importance of this cloud type and its CREs for the domain-
 676 and time-average. Thus, simulated biases in all-sky CREs can arise from biases in (i) the
 677 radiative properties of a given cloud type, and (ii) the cloud cover of a given cloud type.
 678 Biases in radiative properties result from a misrepresentation of the distribution of cloud-
 679 optical thickness which is directly linked to the representation of vertical structure of the
 680 cloud type. Cloud-cover biases provide information on the misrepresentation of the hor-
 681 izontal extent of the respective cloud type. From Fig. 12d, we infer that mainly the four
 682 cloud types "very low / fractional", "low", "mid-level" and "high opaque" (with decreas-
 683 ing importance) contribute to the observed negative net all-sky CREs. The remaining
 684 four cloud types either have near zero net overcast CREs or too little cloud cover. For
 685 simulations with fully parameterized convection, the magnitudes of net all-sky CREs for
 686 very low / fractional and low clouds are severely underestimated. The discrepancy is much
 687 reduced for simulations with shallow convection at 2.5 km grid spacing, especially for
 688 one-moment microphysics. In contrast, the net all-sky CREs of very low / fractional clouds
 689 are overestimated in simulations with fully explicit convection. The all-sky net CREs of
 690 mid-level clouds are better represented for simulations with either shallow or full con-
 691 vection scheme than in simulations with fully explicit convection. In addition, semi. mod-
 692 erately thick clouds have too negative all-sky net CREs in all simulations, with the largest
 693 bias for simulations with fully explicit convection.

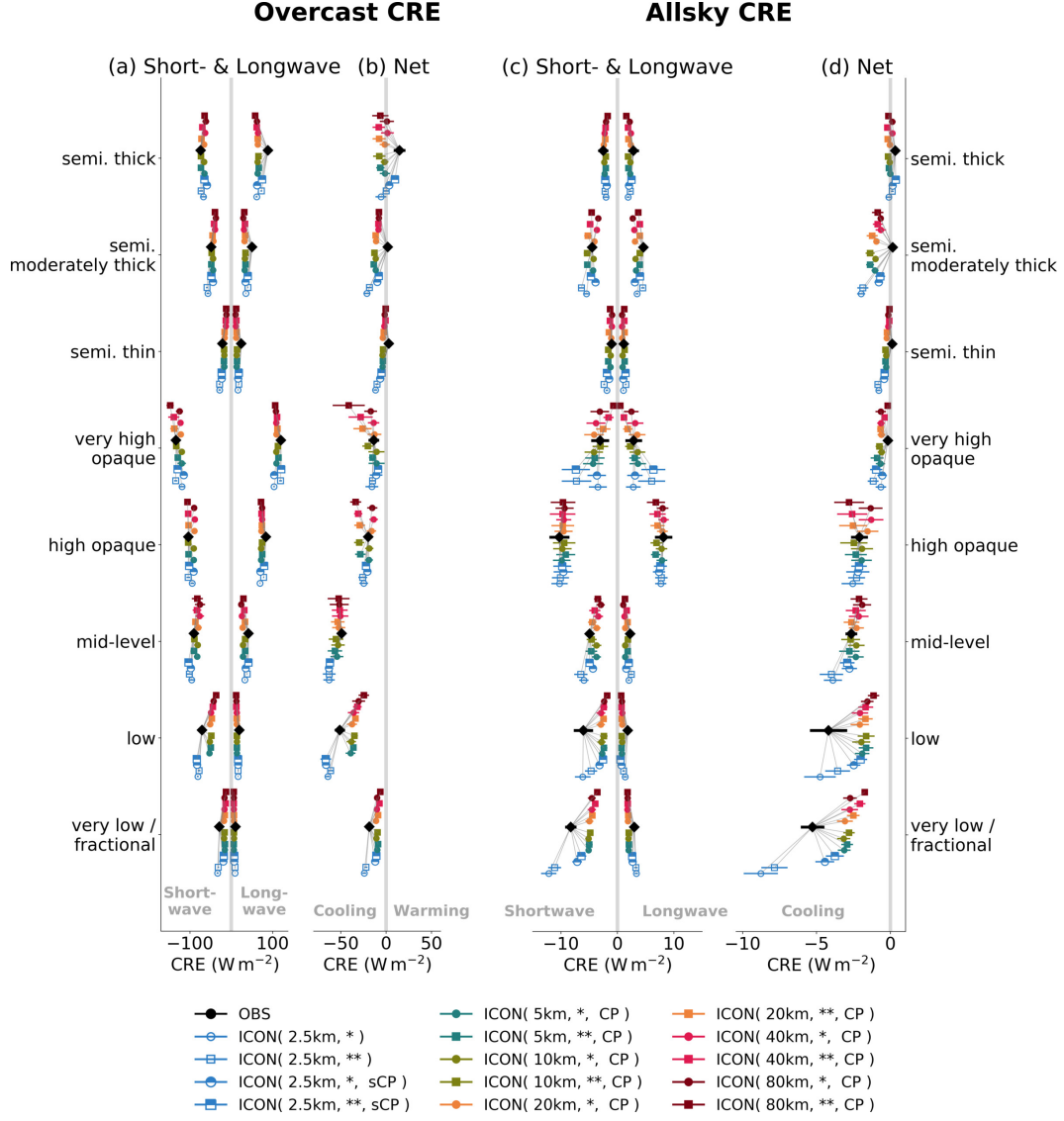


Figure 12. Observed and simulated (a,b) overcast CREs and (c,d) all-sky CREs for different cloud types. Overcast CREs are calculated assuming a hypothetical cloud cover of 100%. All-sky CREs include weighting by the cloud-type’s specific cloud cover. Similar to Fig. 5, symbols denote average values and error bars provide confidence intervals.

To separate the effects of cloud type-dependent cloud cover and radiative properties on biases of simulated all-sky CREs, we apply a bias decomposition to eq. (5),

$$\begin{aligned}
 \delta \text{CRE}_{\text{net}} = & - \underbrace{\sum_{k=0}^K \delta f_k (F_{\text{net},k} - F_{\text{net,clear},k})}_{\text{cloud cover}} - \underbrace{\sum_{k=0}^K f_k \delta (F_{\text{net},k} - F_{\text{net,clear},k})}_{\text{radiative properties}} \\
 & - \underbrace{\sum_{k=0}^K \delta f_k \delta (F_{\text{net},k} - F_{\text{net,clear},k})}_{\text{co-variation}}.
 \end{aligned} \tag{6}$$

694 The first term results from a misrepresentation of cloud cover, the second term from a
 695 misrepresentation of radiative properties and overcast CREs, and the third term from
 696 the co-variation between the two factors. The "cloud cover" term shows how well the
 697 horizontal extend is simulated by cloud type. The "radiation flux" term is related to the
 698 vertical structure of a cloud type. As before, cloud-free contributions are included at $k =$
 699 0 . The decomposition holds for the all-sky net CREs as well as its shortwave and long-
 700 wave components.

701 Fig. 13 summarizes biases in the domain- and time-averaged CREs and their de-
 702 composition. As discussed in Sect. 3.1, net CREs are biased negative for simulations with
 703 explicit convection, i.e. clouds cool too much, but biased positive for simulations with
 704 shallow-convection scheme and fully parameterized convection (except for ICON(2.5km,
 705 *, sCP)), i.e. clouds cool too little. For the latter simulations, net CRE biases become
 706 smaller as the grid spacing is decreased. The compensation of CRE biases originating
 707 in the longwave and shortwave is very apparent for fully convection-parameterized sim-
 708 ulations (Fig. 13a-c).

709 The bias compensation between shortwave and longwave CREs leads to different
 710 roles of cloud cover and radiative properties, depending on whether one looks at net CREs
 711 or their shortwave and longwave components. For net CREs, cloud cover biases dom-
 712 inate. They are responsible for around half of the positive bias for fully parameterized
 713 convection (Fig. 13d). For simulations with fully explicit convection, in contrast, biases
 714 in radiative properties clearly control the net CRE biases. For the shortwave and long-
 715 wave CRE components, biases in radiative properties dominate in general. A pronounced
 716 compensation between shortwave and longwave CRE biases is apparent. We thus find
 717 that the earlier discussed compensation of shortwave and longwave flux biases directly
 718 traces back to a misrepresentation of cloud-radiative properties. Switching from one-moment
 719 to two-moment microphysics has different effects on cloud-cover and radiative-properties
 720 related CRE biases. It is found for nearly all simulations that the shortwave and long-
 721 wave CRE biases due to radiative properties become smaller. For the coarser simulations,
 722 the resulting improvement is more than compensated by biases in the "cloud cover" term.
 723 Thus, the CRE biases become larger when switching to the two-moment scheme in these
 724 coarser ICON experiments (see also Fig. 10e and f). The simulations with shallow-convection
 725 parameterization possess smaller biases than the fully parameterized simulations. The
 726 simulations with fully explicit convection show acceptable results for the longwave bias
 727 due to radiative properties. Their worse net performance originates from the missing com-
 728 pensation by shortwave biases which are also negative for these simulations.

729 The interpretation of CRE biases is further supported by Fig. 14 which provides
 730 a detailed bias decomposition separated by cloud type. We see that not only the com-
 731 pensation between shortwave and longwave CRE biases is important, but also the com-
 732 pensation of biases originating from different cloud types (Klein et al., 2013). For the
 733 net CRE biases (Fig. 14c), mainly cloud types "very low / fractional" and "low" con-
 734 tribute to the positive bias of simulations with fully parameterized convection. This is
 735 partially compensated by a negative net CRE bias from semi. moderately thick clouds.
 736 When split by cloud type, the net CRE bias of simulations with fully parameterized con-
 737 vention is dominated by CRE biases due to radiative properties.

738 For shortwave and longwave CRE biases (Fig. 14a,b), it is found that the resolu-
 739 tion dependence of CRE biases not only originates from very low / fractional and low
 740 clouds, but also from very high opaque clouds. This cloud type is connected to deep con-
 741 vection which representation significantly improves for decreasing grid spacing. Espe-
 742 cially, some simulations with two-moment microphysics show a rather poor performance
 743 for the very high opaque clouds. The coarse simulation at 80 km underestimates the frac-
 744 tional coverage of this cloud type, in contrast the simulation with shallow convection pa-
 745 rameterization at 2.5 km overestimates the fractional coverage of very high opaque clouds
 746 (see also Fig. 11b). The spatial representation of this cloud type needs to be addressed

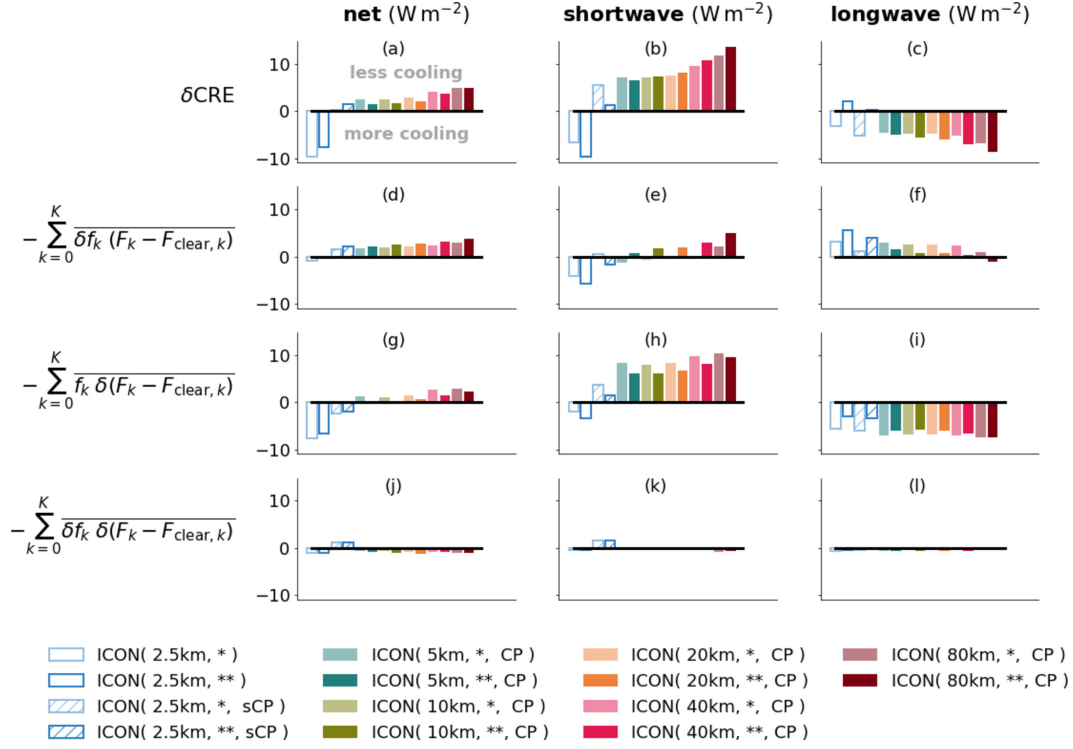


Figure 13. Decomposition of CRE biases (1st row) into contributions from biases in cloud cover (2nd row) and cloud-radiative properties (3rd row). Co-variations between biases in cloud cover and radiative properties are shown in the 4th row. The net CRE biases (left column) are decomposed into shortwave and longwave (middle and right columns) contributions.

747 In future. In the shortwave, the positive CRE bias of simulations with fully parameter-
 748 ized convection mainly comes from very low / fractional and low clouds. For the former,
 749 biases in radiative properties dominate whereas for the latter CRE biases due to cloud
 750 cover also contribute. Switching from one-moment to two-moment scheme, we find im-
 751 provements in the representation of shortwave components of individual radiative prop-
 752 erties (see Fig. 13h and Fig. 14g) which indicate that the vertical structure of clouds in
 753 terms of optical thicknesses has improved. These improvements are partially masked by
 754 worse cloud cover biases (see Fig. 13e). In the longwave, many cloud types simulated with
 755 fully parameterized convection show a negative bias originating from the bias in radi-
 756 ative properties. The magnitudes of the individual longwave biases are much smaller for
 757 simulations with explicit convection.

758 In summary, the above analysis showed that future model development should equally
 759 concentrate on improvements of simulated clear-sky and cloud-affected TOA radiation
 760 fluxes. For the former, we recommend to revise the formulation of ocean albedo to reach
 761 better consistency with observations. For CREs, strategies for further improvement de-
 762 pend on the choice of the convection scheme, especially at kilometer-scale resolutions.
 763 For simulations with fully parameterized convection, radiation is typically too weakly
 764 interacting with clouds, i.e. clouds appear too dark and too warm, especially for low and
 765 very low / fractional clouds. Hence, in contrast to the well known “too few, too bright”
 766 low-cloud problem of several climate models (Nam et al., 2012; Klein et al., 2013), low
 767 and very low clouds in ICON at coarse resolutions need to become brighter. This could
 768 be achieved by improving radiative properties of these cloud types, either from a macro-
 769 physical or a microphysical point of view. Specifically, in the used ICON version the ef-

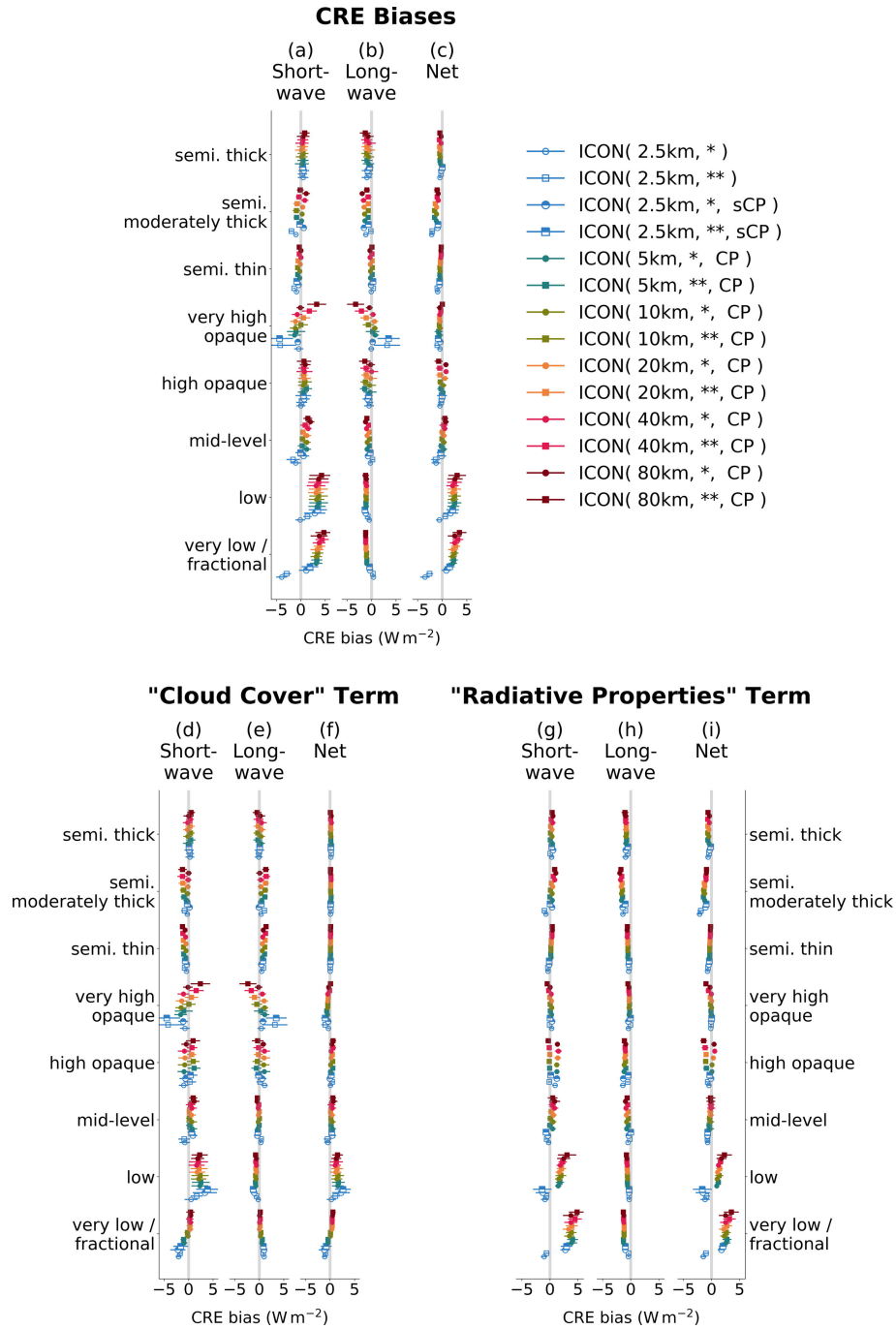


Figure 14. CRE biases and their decomposition for different cloud types. Following eq. (6), (top row) biases in CREs are separated into (bottom row) contribution from (left) cloud-cover biases and (right) radiation-flux biases. The split into (a, d, g) shortwave and (b, e, h) longwave components that sum up to the (c, f, i) net CRE bias is also provided in the different sub-panels. Similar to Fig. 5, symbols denote average values and error bars provide confidence intervals.

770 fective radius of cloud particles taken in the radiative transfer follows from a prescribed
 771 number concentration of cloud particles and is unaware of the number concentration sim-
 772 ulated by the two-moment microphysics scheme. Adjusting this inconsistency might help

773 to correct the CRE biases, e.g. the negative biases in longwave CREs of semi-transparent
 774 cirrus. For simulations with only shallow or fully explicit convection, the radiative prop-
 775 erties of clouds show signs of improvement. However, ICON with shallow convection sim-
 776 ulates very low clouds, which still appear too dark and too similar to the clouds from
 777 the fully parameterized convection simulations. To improve the representation of this
 778 cloud type, new parameterization approaches need to be explored, such as those using
 779 stochastic sampling (Sakradzija & Klocke, 2018). The simulations with explicit convec-
 780 tion show a promising convergence, which should be investigated by further refinements
 781 down to the hectometer-scale (Stevens et al., 2020).

782 4 Conclusions and Outlook

783 Clouds regulate Earth’s energy budget (Ramanathan et al., 1989). Shallow low-
 784 level clouds are efficient scatterers of shortwave radiation and, in combination with their
 785 small thermal contrast to Earth’s surface, they have strong negative cloud-radiative ef-
 786 fects and cool the Earth. In contrast, the cloud-radiative effects of high-level cirrus clouds
 787 also include longwave effects so that depending on cirrus-optical properties these clouds
 788 can either have a near zero or a warming effect (G. L. Stephens, 2005).

789 In mid-latitude environments, cyclones lead to the formation of frontal cloud bands
 790 with a complicated mixture of stratiform and convective clouds, possibly including multi-
 791 layer structures and embedded convection. Realistically representing such complex cloud
 792 structures and their radiative effects poses a challenge to numerical models, especially
 793 over oceans where extended shallow boundary-layer cloud fields occur in addition. Fur-
 794 thermore, the radiative impact of clouds on the mid-latitude circulation might depend
 795 on cloud type. We therefore investigated the ability of a specific numerical weather pre-
 796 diction - the ICON model (Zängl et al., 2014) - to represent cloud cover and cloud-radiative
 797 effects for selected days of the NAWDEX field campaign in boreal autumn 2016 over a
 798 large North Atlantic domain. Using a comprehensive set of sensitivity simulations that
 799 vary horizontal grid spacing between 2.5 and 80 km, we identified sensitivities with re-
 800 spect to model resolution. Moreover, we studied the impact of different choices regard-
 801 ing the parameterization of cloud microphysics (one-moment versus two-moment scheme)
 802 and convection (fully parameterized, shallow-convection only, fully explicit). This allowed
 803 us to identify strengths and weaknesses of the different model setups, in particular with
 804 respect to top-of-atmosphere radiation fluxes and cloud-radiative effects.

805 To assess the ICON model we made use of multi-spectral observations from the geo-
 806 stationary Meteosat satellite in two ways. First, we analyzed observational estimates of
 807 instantaneous top-of-atmosphere radiation. Second, we derived a detailed multi-spectral
 808 cloud classification from the Meteosat observations. For a consistent comparison between
 809 the ICON simulations and the observations, the simulation data were forwarded to a satel-
 810 lite forward operator performing radiative transfer calculations to derive synthetic in-
 811 frared satellite images. This transfer of the simulations to observation space allowed us
 812 to subject simulations and observations to the same cloud classification software, and
 813 to analyze and compare observed and simulated cloud-type fields within the same frame-
 814 work.

815 In observations, the average net TOA radiation flux over the North Atlantic region
 816 and for the selected analysis days is around $+25 \text{ W m}^{-2}$, indicating a net energy loss (re-
 817 member that we adopted a positive-upward convention for radiation fluxes). Clouds sub-
 818 stantially contribute to the energy loss and are responsible for a net cooling of -14 W m^{-2} .
 819 Major contributors to the net CRE are shallow clouds of the cloud type ”very low / frac-
 820 tional” and ”low”, which both contribute around -5 W m^{-2} to the total net CRE. The
 821 shallow clouds also account for around half of the total cloud cover of 73%.

822 The main results of our comparison between observed and ICON simulated radi-
 823 ation fluxes and cloud fields are as follows:

- 824 (i) For all model setups, the domain- and time-averaged net TOA radiation flux is larger
 825 than in the observations, independent of resolution and the treatment of cloud mi-
 826 crophysics and convection. The ICON model thus overestimates the TOA loss of
 827 radiative energy. Simulations with fully parameterized convection underestimate
 828 TOA shortwave reflection and overestimate outgoing longwave radiation, i.e. seen
 829 from space they are too dark and too warm.
- 830 (ii) There is a systematic bias compensation between shortwave reflection and outgo-
 831 ing longwave radiation. The compensation is stronger for coarse-resolution simu-
 832 lations and becomes smaller for finer resolutions. Clear-sky and CRE biases have
 833 similar magnitudes, but only CRE biases are sensitive to horizontal resolution and
 834 in fact decrease with finer resolution. For fully parameterized-convection simula-
 835 tions, clouds are too weakly interacting with the radiation field leading to positive
 836 CRE biases in the shortwave and negative CRE biases in the longwave which par-
 837 tially compensate each other.
- 838 (iii) For none of the ICON setups, a simultaneous match between observed and sim-
 839 ulated CREs and total cloud cover is achieved. Cloud cover compares better to ob-
 840 servations for coarse resolutions, whereas CREs compares better to observations
 841 for finer resolutions.
- 842 (iv) The cloud cover of shallow clouds (types: “very low / fractional” and “low”) strongly
 843 depends on resolution. It compares well with observations for coarser resolutions
 844 of 10-80 km, but finer resolutions and explicit convection severely overestimate it
 845 by up to 50% relative to observations. For simulations with fully parameterized con-
 846 vection, net CRE-biases of shallow clouds are dominated by positive shortwave bi-
 847 ases in radiative properties. Biases in shortwave and net CREs are reduced when
 848 only shallow convection parameterization is applied. Using explicit convection even
 849 switches the sign of the shortwave CRE-biases leading to too bright shallow clouds
 850 and too large cloud-induced reflection.
- 851 (v) The choice of the microphysics scheme has dominant impact on cloud cover of cir-
 852 rus clouds leading to smaller cloud cover for high opaque and very high opaque clouds
 853 and larger cloud cover for semi. thin and semi. moderately thick clouds. No pro-
 854 nounced net warming effect is found for simulated semi-transparent clouds. The
 855 net CRE bias of semi-transparent clouds is negative and caused by a misrepresenta-
 856 tion of cirrus radiative properties, especially in the longwave.

857 In summary, our analysis shows that refining horizontal resolution allows the ICON
 858 model to more accurately represent cloud-radiative effects over the North Atlantic. We
 859 found substantial bias compensation between top-of-atmosphere shortwave and longwave
 860 radiation fluxes as well as between clear-sky fluxes and cloud-radiative effects. An ac-
 861 ceptable net performance of a selected model setup is not at all a guarantor of realistic
 862 individual contributions. The best representation of the domain-average longwave and
 863 shortwave CREs is achieved when ICON is configured with two-moment cloud micro-
 864 physics, a shallow-convection scheme (explicit treatment of mid-level and deep convec-
 865 tion) and a horizontal resolution of 2.5 km.

866 Starting with climate model resolution of 80 km, the improvement from increas-
 867 ing resolution are gradually up to a resolution of 10 to 20 km, at which point a further
 868 increase in resolution only leads small and insufficient improvements of the simulated short-
 869 wave CREs. Instead, at finer resolutions, the saturation is overcome when the convec-
 870 tion scheme is disabled so that the model is allowed to represent convection in an explicit
 871 manner. If convection treated explicitly, the simulation of CREs is even improved by re-
 872 finements at (and possibly beyond) the kilometer scale. However, a resolution of 2.5 km
 873 is still too coarse to resolve the shallow clouds and circulation in the marine boundary

874 layer, because of which the best simulation of average CREs at 2.5 km is achieved with
 875 an explicit treatment of mid-level and deep convection but a parameterized treatment
 876 of shallow convection. This simulation setup can represent the radiative-properties term
 877 in the CRE decomposition in a satisfactory manner for all cloud types except for very
 878 low clouds. For this cloud type, improvements in the simulation of cloud-optical thick-
 879 ness and thus vertical structure is needed. Moreover, the 2.5-km setup with parameter-
 880 ized shallow convection shows some deficits with regard to the fractional coverage of cloud
 881 types "very high opaque" and "low" which could be an indication that the linking be-
 882 tween resolved and parameterized convection has weaknesses in this setup. Compared
 883 to fully explicit convection, the use of a shallow-convection scheme mitigates the oth-
 884 erwise too high fractional coverage of very low clouds and too strong cloud shortwave
 885 reflection, and at the same time does not affect longwave CRE, which are dominated by
 886 high-level clouds. A deeper understanding of the spatial distribution of the CRE biases
 887 is needed. A promising approach would be the analysis of the cloud distribution and its
 888 radiative effects as a function of meteorological conditions, e.g. cloud controlling factors
 889 depending on large-scale circulation and vertical velocity regimes.

890 Acknowledgments

891 FS and AV are supported by the German Ministry of Education and Research (BMBF)
 892 and FONA: Research for Sustainable Development (www.fona.de). This work contributes
 893 to the WCRP's Grand Challenge on Clouds, Circulation, and Climate Sensitivity and
 894 the BMBF-funded project HD(CP)² : High Definition Clouds and Precipitation for Ad-
 895 vancing Climate Prediction. FS acknowledges funding under respective grants 01LK1507C
 896 and 01LK1503F, AV is supported under Grant Agreement 01LK1509A. The ICON sim-
 897 ulations were performed by AV at the DKRZ in Hamburg, Germany, which is thanked
 898 for its support. We also thank EUMETSAT for producing the SEVIRI data, which have
 899 been obtained from the TROPOS satellite data archive.

900 Concerning data availability: The GERB-like data is made freely available to the
 901 user community via the RMIB OnLine Shortterm Service (ROLSS, see <ftp://gerb.oma.be>)
 902 server, after registration. The primary data of the ICON simulations (run scripts, namelists,
 903 scripts for lateral boundary data) will be published at KITopen of Karlsruhe Institute
 904 of Technology. Analysis data have been collected at the long-term archive (LTA) of DKRZ
 905 and can be assessed under [https://cera-www.dkrz.de/WDC/ui/ceraresearch/entry](https://cera-www.dkrz.de/WDC/ui/ceraresearch/entry?acronym=DKRZ_LTA_834_ds00048)
 906 [?acronym=DKRZ_LTA_834_ds00048](https://cera-www.dkrz.de/WDC/ui/ceraresearch/entry?acronym=DKRZ_LTA_834_ds00048).

907 Open science: The analysis source code has been made freely available to improve
 908 reproducibility of our results. Basic analysis tools are written in Python and published
 909 at <http://doi.org/10.5281/zenodo.3657387>. The final plots for our paper were done with
 910 Jupyter Notebooks which are hosted at [https://github.com/fsenf/nbook.CRE-2020-paper-](https://github.com/fsenf/nbook.CRE-2020-paper-plots)
 911 [plots](https://github.com/fsenf/nbook.CRE-2020-paper-plots).

912 References

- 913 Albern, N., Voigt, A., & Pinto, J. G. (2019). Cloud-radiative impact on the regional
 914 responses of the midlatitude jet streams and storm tracks to global warming.
 915 *J. Adv. Model. Earth Syst.*, *11*(7), 1940-1958.
- 916 Allan, R. P. (2011). Combining satellite data and models to estimate cloud radiative
 917 effect at the surface and in the atmosphere. *Meteorological Applications*, *18*(3),
 918 324-333.
- 919 Arking, A. (1991). The radiative effects of clouds and their impact on climate. *Bull.*
 920 *Amer. Meteor. Soc.*, *72*(6), 795-814.
- 921 Baldauf, M., Seifert, A., Förstner, J., Majewski, D., Raschendorfer, M., & Rein-
 922 hardt, T. (2011). Operational convective-scale numerical weather prediction

- 923 with the cosmo model: Description and sensitivities. *Mon. Wea. Rev.*, *139*(12),
924 3887-3905.
- 925 Bechtold, P., Köhler, M., Jung, T., Doblas-Reyes, F., Leutbecher, M., Rodwell,
926 M. J., ... Balsamo, G. (2008). Advances in simulating atmospheric variability
927 with the ECMWF model: From synoptic to decadal time-scales. *Quarterly*
928 *Journal of the Royal Meteorological Society: A journal of the atmospheric*
929 *sciences, applied meteorology and physical oceanography*, *134*(634), 1337–1351.
- 930 Bodas-Salcedo, A., Williams, K. D., Ringer, M. A., Beau, I., Cole, J. N. S.,
931 Dufresne, J. L., ... Yokohata, T. (2014, Jan). Origins of the Solar Radiation
932 Biases over the Southern Ocean in CFMIP2 Models*. *J. Climate*, *27*(1),
933 41-56. doi: 10.1175/JCLI-D-13-00169.1
- 934 Bodas-Salcedo, A., Webb, M. J., Bony, S., Chepfer, H., Dufresne, J.-L., Klein, S. A.,
935 ... et al. (2011). COSP: Satellite simulation software for model assessment.
936 *Bull. Amer. Meteor. Soc.*, *92*(8), 1023-1043.
- 937 Böhme, T., Stapelberg, S., Akkermans, T., Crewell, S., Fischer, J., Reinhardt, T.,
938 ... van Lipzig, N. (2011, April). Long-term evaluation of COSMO forecast-
939 ing using combined observational data of the GOP period. *Meteor. Z.*, *20*,
940 119-132. doi: 10.1127/0941-2948/2011/0225
- 941 Boucher, O., Randall, D., Artaxo, P., Bretherton, C., Feingold, G., Forster, P., ... et
942 al. (2013). Clouds and aerosols. In *Climate change 2013: The physical science*
943 *basis. contribution of working group i to the fifth assessment report of the in-*
944 *tergovernmental panel on climate change* (pp. 571–657). Cambridge University
945 Press.
- 946 Ceppi, P., Brient, F., Zelinka, M. D., & Hartmann, D. L. (2017). Cloud feedback
947 mechanisms and their representation in global climate models. *Wiley Interdis-*
948 *cip. Rev. Clim. Change*, *8*(4), e465.
- 949 Ceppi, P., & Hartmann, D. L. (2015). Connections between clouds, radiation, and
950 midlatitude dynamics: a review. *Curr. Clim. Change Rep.*, *1*(2), 94-102.
- 951 Ceppi, P., & Hartmann, D. L. (2016). Clouds and the atmospheric circulation re-
952 sponse to warming. *J. Climate*, *29*(2), 783-799.
- 953 Ceppi, P., & Shepherd, T. G. (2017, Nov). Contributions of Climate Feedbacks to
954 Changes in Atmospheric Circulation. *J. Climate*, *30*(22), 9097-9118. doi: 10
955 .1175/JCLI-D-17-0189.1
- 956 Chaboureaud, J.-P., Cammas, J.-P., Mascart, P., Pinty, J.-P., Claud, C., Roca, R.,
957 & Morcrette, J.-J. (2000). Evaluation of a cloud system life-cycle simulated
958 by the Meso-NH model during FASTEX using METEOSAT radiances and
959 TOVS-3I cloud retrievals. *Quart. J. Roy. Meteor. Soc.*, *126*(566), 1735-1750.
- 960 Chen, T., Rossow, W. B., & Zhang, Y. (2000). Radiative effects of cloud-type varia-
961 tions. *J. Climate*, *13*(1), 264-286.
- 962 Clerbaux, N., Bertrand, C., Caprion, D., Depaepe, B., Dewitte, S., Gonzalez, L., &
963 Ipe, A. (2005). Narrowband-to-broadband conversions for seviri. In *Proc. of*
964 *the 2005 eumetsat meteorological satellite conference* (p. 351-357).
- 965 Collins, M., Minobe, S., Barreiro, M., Bordoni, S., Kaspi, Y., Kuwano-Yoshida, A.,
966 ... others (2018). Challenges and opportunities for improved understanding of
967 regional climate dynamics. *Nature Climate Change*, *8*(2), 101.
- 968 Derrien, M., & Le Gléau, H. (2005). MSG/SEVIRI cloud mask and type
969 from SAFNWC. *Int. J. Remote Sens.*, *26*, 4707-4732. doi: 10.1080/
970 01431160500166128
- 971 Dewitte, S., Gonzalez, L., Clerbaux, N., Ipe, A., Bertrand, C., & Paepe, B. D.
972 (2008). The geostationary earth radiation budget edition 1 data processing
973 algorithms. *Adv. Space Res.*, *41*(11), 1906 - 1913.
- 974 Dolinar, E. K., Dong, X., Xi, B., Jiang, J. H., & Su, H. (2015). Evaluation of cmip5
975 simulated clouds and toa radiation budgets using nasa satellite observations.
976 *Climate Dyn.*, *44*(7-8), 2229–2247.
- 977 Eikenberg, S., Khler, C., Seifert, A., & Crewell, S. (2015, Apr). How microphysical

- 978 choices affect simulated infrared brightness temperatures. *Atmos. Res.*, *156*,
 979 6779. Retrieved from <http://dx.doi.org/10.1016/j.atmosres.2014.12.010>
 980 doi: 10.1016/j.atmosres.2014.12.010
- 981 Evans, S., Marchand, R., Ackerman, T., Donner, L., Golaz, J.-C., & Seman, C.
 982 (2017). Diagnosing cloud biases in the gfdl am3 model with atmospheric
 983 classification. *J. Geophys. Res. Atmos.*, *122*(23), 12,827-12,844.
- 984 Fu, Q. (1996). An Accurate Parameterization of the Solar Radiative Properties of
 985 Cirrus Clouds for Climate Models. *J. Climate*, *9*, 2058-2082.
- 986 Futyan, J. M., & Russell, J. E. (2005). Developing clear-sky flux products for the
 987 geostationary earth radiation budget experiment. *J. Appl. Meteor.*, *44*(9),
 988 1361-1374.
- 989 Gettelman, A., & Sherwood, S. C. (2016). Processes responsible for cloud feedback.
 990 *Curr. Clim. Change Rep.*, *2*(4), 179-189.
- 991 Grise, K. M., Medeiros, B., Benedict, J. J., & Olson, J. G. (2019). Investigating the
 992 influence of cloud radiative effects on the extratropical storm tracks. *Geophys.*
 993 *Res. Lett.*, *46*(13), 7700-7707.
- 994 Grise, K. M., & Polvani, L. M. (2014, Aug). Southern Hemisphere Cloud-Dynamics
 995 Biases in CMIP5 Models and Their Implications for Climate Projections. *J.*
 996 *Climate*, *27*(15), 6074-6092. doi: 10.1175/JCLI-D-14-00113.1
- 997 Haarsma, R. J., Roberts, M. J., Vidale, P. L., Senior, C. A., Bellucci, A., Bao, Q.,
 998 ... von Storch, J.-S. (2016). High resolution model intercomparison project
 999 (highresmip v1.0) for cmip6. *Geosci. Model Dev.*, *9*(11), 4185-4208.
- 1000 Harries, J. E., Russell, J. E., Hanafin, J. A., Brindley, H., Futyan, J., Rufus, J., ...
 1001 Ringer, M. A. (2005). The geostationary earth radiation budget project. *Bull.*
 1002 *Amer. Meteor. Soc.*, *86*(7), 945-960.
- 1003 Hartmann, D. L., Ockert-Bell, M. E., & Michelsen, M. L. (1992). The effect of cloud
 1004 type on earth's energy balance: Global analysis. *J. Climate*, *5*(11), 1281-1304.
- 1005 Heinze, R., Dipankar, A., Carbajal Henken, C., Moseley, C., Sourdeval, O., Trömel,
 1006 S., ... Quaas, J. (2017). Large-eddy simulations over germany using ICON: a
 1007 comprehensive evaluation. *Quart. J. Roy. Meteor. Soc.*, *143*(702), 69-100.
- 1008 Henderson, D. S., L'Ecuyer, T., Stephens, G., Partain, P., & Sekiguchi, M. (2013).
 1009 A multisensor perspective on the radiative impacts of clouds and aerosols. *J.*
 1010 *Appl. Meteor. Climatol.*, *52*(4), 853-871.
- 1011 Hogan, R. J., & Illingworth, A. J. (2000). Deriving cloud overlap statistics from
 1012 radar. *Quart. J. Roy. Meteor. Soc.*, *126*(569), 2903-2909.
- 1013 Hohenegger, C., Kornblüh, L., Klocke, D., Becker, T., Cioni, G., Engels, J. F., ...
 1014 Stevens, B. (2020). Climate statistics in global simulations of the atmosphere,
 1015 from 80 to 2.5 km grid spacing. *J. Meteor. Soc. Japan*, *98*(1), 73-91. doi:
 1016 10.2151/jmsj.2020-005
- 1017 Hollingsworth, A., Engelen, R. J., Textor, C., Benedetti, A., Boucher, O., Chevallier,
 1018 F., ... Consortium, T. G. (2008, 08). Toward a Monitoring and Forecasting
 1019 System for Atmospheric Composition: The GEMS Project. *Bull. Amer.*
 1020 *Meteor. Soc.*, *89*(8), 1147-1164. Retrieved from [https://doi.org/10.1175/](https://doi.org/10.1175/2008BAMS2355.1)
 1021 [2008BAMS2355.1](https://doi.org/10.1175/2008BAMS2355.1) doi: 10.1175/2008BAMS2355.1
- 1022 Keil, C., Tafferner, A., & Reinhardt, T. (2006). Synthetic satellite imagery in the
 1023 Lokal-Modell. *Atmos. Res.*, *82*, 19-25.
- 1024 Klein, S. A., Zhang, Y., Zelinka, M. D., Pincus, R., Boyle, J., & Gleckler, P. J.
 1025 (2013). Are climate model simulations of clouds improving? an evaluation
 1026 using the isccp simulator. *J. Geophys. Res. Atmos.*, *118*(3), 1329-1342.
 1027 Retrieved from [https://agupubs.onlinelibrary.wiley.com/doi/abs/](https://agupubs.onlinelibrary.wiley.com/doi/abs/10.1002/jgrd.50141)
 1028 [10.1002/jgrd.50141](https://doi.org/10.1002/jgrd.50141) doi: 10.1002/jgrd.50141
- 1029 Klocke, D., Brueck, M., Hohenegger, C., & Stevens, B. (2017). Rediscovery of the
 1030 doldrums in storm-resolving simulations over the tropical Atlantic. *Nature*
 1031 *Geoscience*, *10*(12), 891-896.
- 1032 Köhler, C. G., & Seifert, A. (2015, Feb). Identifying sensitivities for cirrus modelling

- 1033 using a two-moment two-mode bulk microphysics scheme. *Tellus B*, 67(0). Re-
 1034 trieved from <http://dx.doi.org/10.3402/tellusb.v67.24494> doi: 10.3402/
 1035 tellusb.v67.24494
- 1036 L'Ecuyer, T. S., Hang, Y., Matus, A. V., & Wang, Z. (2019). Reassessing the effect
 1037 of cloud type on earth's energy balance in the age of active spaceborne obser-
 1038 vations. part i: Top of atmosphere and surface. *J. Climate*, 32(19), 6197-6217.
- 1039 Li, Y., Thompson, D. W. J., Bony, S., & Merlis, T. M. (2019, Feb). Thermodynamic
 1040 Control on the Poleward Shift of the Extratropical Jet in Climate Change
 1041 Simulations: The Role of Rising High Clouds and Their Radiative Effects. *J.*
 1042 *Climate*, 32(3), 917-934. doi: 10.1175/JCLI-D-18-0417.1
- 1043 Maher, P., Vallis, G. K., Sherwood, S. C., Webb, M. J., & Sansom, P. G. (2018).
 1044 The impact of parameterized convection on climatological precipitation in
 1045 atmospheric global climate models. *Geophys. Res. Lett.*, 45(8), 3728-3736.
- 1046 Matricardi, M., Chevallier, F., Kelly, G., & Thépaut, J.-N. (2004). An improved
 1047 general fast radiative transfer model for the assimilation of radiance observa-
 1048 tions. *Quart. J. Roy. Meteor. Soc.*, 130, 153-173.
- 1049 Matsui, T., Dolan, B., Rutledge, S. A., Tao, W.-K., Iguchi, T., Barnum, J., & Lang,
 1050 S. E. (2019). Polarris: A polarimetric radar retrieval and instrument simula-
 1051 tor. *J. Geophys. Res. Atmos.*, 124(8), 4634-4657. Retrieved from [https://](https://agupubs.onlinelibrary.wiley.com/doi/abs/10.1029/2018JD028317)
 1052 agupubs.onlinelibrary.wiley.com/doi/abs/10.1029/2018JD028317 doi:
 1053 10.1029/2018JD028317
- 1054 McDonald, A. J., & Parsons, S. (2018). A comparison of cloud classification method-
 1055 ologies: Differences between cloud and dynamical regimes. *J. Geophys. Res.*
 1056 *Atmos.*, 123(19), 11,173-11,193.
- 1057 McFarquhar, G. M., Iacobellis, S., & Somerville, R. C. J. (2003). SCM Simula-
 1058 tions of Tropical Ice Clouds Using Observationally Based Parameterizations of
 1059 Microphysics. *J. Climate*, 16(11), 1643-1664.
- 1060 Meirink, J. F., Roebeling, R. A., & Stammes, P. (2013). Inter-calibration of polar
 1061 imager solar channels using seviri. *Atmos. Meas. Tech.*, 6(9), 2495-2508.
- 1062 Mekaoui, S., & Dewitte, S. (2008). Total Solar Irradiance Measurement and Mod-
 1063 elling during Cycle 23. *Sol. Phys.*, 247(1), 203-216.
- 1064 Mlawer, E. J., Taubman, S. J., Brown, P. D., Iacono, M. J., & Clough, S. A. (1997).
 1065 Radiative transfer for inhomogeneous atmospheres: RRTM, a validated
 1066 correlated-k model for the longwave. *J. Geophys. Res. Atmos.*, 102(D14),
 1067 16663-16682.
- 1068 Morcrette, J.-J. (1991). Evaluation of Model-generated Cloudiness: Satellite-
 1069 observed and Model-generated Diurnal Variability of Brightness Temperature.
 1070 *Mon. Wea. Rev.*, 119(5), 1205-1224.
- 1071 Nam, C., Bony, S., Dufresne, J.-L., & Chepfer, H. (2012). The "too few, too bright"
 1072 tropical low-cloud problem in cmip5 models. *Geophys. Res. Lett.*, 39(21).
- 1073 Ockert-Bell, M. E., & Hartmann, D. L. (1992). The effect of cloud type on earth's
 1074 energy balance: Results for selected regions. *J. Climate*, 5(10), 1157-1171.
- 1075 Oreopoulos, L., Cho, N., Lee, D., & Kato, S. (2016). Radiative effects of global
 1076 modis cloud regimes. *J. Geophys. Res. Atmos.*, 121(5), 2299-2317.
- 1077 Oreopoulos, L., & Rossow, W. B. (2011). The cloud radiative effects of interna-
 1078 tional satellite cloud climatology project weather states. *J. Geophys. Res. At-*
 1079 *mos.*, 116(D12).
- 1080 Pincus, R., Platnick, S., Ackerman, S. A., Hemler, R. S., & Patrick Hofmann, R. J.
 1081 (2012). Reconciling simulated and observed views of clouds: Modis, isccp, and
 1082 the limits of instrument simulators. *J. Climate*, 25(13), 4699-4720.
- 1083 Prein, A. F., Langhans, W., Fossier, G., Ferrone, A., Ban, N., Goergen, K., ... Le-
 1084 ung, R. (2015). A review on regional convection-permitting climate modeling:
 1085 Demonstrations, prospects, and challenges. *Rev. Geophys.*, 53(2), 323-361.
- 1086 Pscheidt, I., Senf, F., Heinze, R., Deneke, H., Trömel, S., & Hohenegger, C. (2019).
 1087 How organized is deep convection over germany? *Quart. J. Roy. Meteor. Soc.*,

- 1088 145(723), 2366-2384.
- 1089 Ramanathan, V., Cess, R., Harrison, E., Minnis, P., Barkstrom, B., Ahmad, E., &
1090 Hartmann, D. (1989). Cloud-radiative forcing and climate: Results from the
1091 earth radiation budget experiment. *Science*, 243(4887), 57-63.
- 1092 Randall, D., Khairoutdinov, M., Arakawa, A., & Grabowski, W. (2003). Breaking
1093 the cloud parameterization deadlock. *Bull. Amer. Meteor. Soc.*, 84(11), 1547-
1094 1564.
- 1095 Ritter, B., & Geleyn, J.-F. (1992). A comprehensive radiation scheme for numerical
1096 weather prediction models with potential applications in climate simulations.
1097 *Mon. Wea. Rev.*, 120(2), 303-325.
- 1098 Roberts, M. J., Vidale, P. L., Senior, C., Hewitt, H. T., Bates, C., Berthou, S., ...
1099 Wehner, M. F. (2018). The benefits of global high resolution for climate simu-
1100 lation: Process understanding and the enabling of stakeholder decisions at the
1101 regional scale. *Bull. Amer. Meteor. Soc.*, 99(11), 2341-2359.
- 1102 Roca, R., Picon, L., Desbois, M., Le Treut, H., & Morcrette, J.-J. (1997). Direct
1103 comparison of meteosat water vapor channel data and general circulation
1104 model results. *Geophys. Res. Lett.*, 24(2), 147-150.
- 1105 Rossow, W. B., & Schiffer, R. A. (1999). Advances in understanding clouds from is-
1106 ccip. *Bull. Amer. Meteor. Soc.*, 80(11), 2261-2287.
- 1107 Sakradzija, M., & Klocke, D. (2018). Physically constrained stochastic shallow
1108 convection in realistic kilometer-scale simulations. *J. Adv. Model. Earth Syst.*,
1109 10(11), 2755-2776. Retrieved from [https://agupubs.onlinelibrary.wiley](https://agupubs.onlinelibrary.wiley.com/doi/abs/10.1029/2018MS001358)
1110 [.com/doi/abs/10.1029/2018MS001358](https://agupubs.onlinelibrary.wiley.com/doi/abs/10.1029/2018MS001358) doi: 10.1029/2018MS001358
- 1111 Satoh, M., Noda, A. T., Seiki, T., Chen, Y.-W., Kodama, C., Yamada, Y., ... Sato,
1112 Y. (2018). Toward reduction of the uncertainties in climate sensitivity due to
1113 cloud processes using a global non-hydrostatic atmospheric model. *Prog. Earth*
1114 *Planet. Sci.*, 5(1), 67.
- 1115 Satoh, M., Stevens, B., Judt, F., Khairoutdinov, M., Lin, S.-J., Putman, W. M., &
1116 Düben, P. (2019, 17). Global cloud-resolving models. *Curr. Clim. Change*
1117 *Rep.*
- 1118 Saunders, R., Matricardi, M., & Brunel, P. (1999). An improved for assimilation
1119 of satellite radiance observations. *Quart. J. Roy. Meteor. Soc.*, 125(556), 1407-
1120 1425.
- 1121 Schäfer, S. A. K., & Voigt, A. (2018, Mar). Radiation Weakens Idealized Mid-
1122 latitude Cyclones. *Geophys. Res. Lett.*, 45(6), 2833-2841. doi: 10.1002/
1123 2017GL076726
- 1124 Schäfler, A., Craig, G., Wernli, H., Arbogast, P., Doyle, J. D., McTaggart-Cowan,
1125 R., ... Zinner, T. (2018). The north atlantic waveguide and downstream
1126 impact experiment. *Bull. Amer. Meteor. Soc.*, 99(8), 1607-1637.
- 1127 Schmetz, J., Pili, P., Tjemkes, S., Just, D., Kerkmann, J., Rota, S., & Ratier, A.
1128 (2002). An introduction to Meteosat Second Generation (MSG). *Bull. Amer.*
1129 *Meteor. Soc.*, 83(7), 977-992.
- 1130 Seifert, A., & Beheng, K. D. (2006, 01). A two-moment cloud microphysics param-
1131 eterization for mixed-phase clouds. part 1: Model description. *Meteor. Atmos.*
1132 *Phys.*, 92(1), 45-66.
- 1133 Senf, F., & Deneke, H. (2017). Uncertainties in synthetic meteosat sevir infrared
1134 brightness temperatures in the presence of cirrus clouds and implications for
1135 evaluation of cloud microphysics. *Atmos. Res.*, 183, 113-129.
- 1136 Senf, F., Klocke, D., & Brueck, M. (2018). Size-resolved evaluation of simulated
1137 deep tropical convection. *Mon. Wea. Rev.*, 146(7), 2161-2182.
- 1138 Sohn, B. J., Nakajima, T., Satoh, M., & Jang, H. S. (2010, December). Impact of
1139 different definitions of clear-sky flux on the determination of longwave cloud
1140 radiative forcing: NICAM simulation results. *Atmos. Chem. Phys.*, 10(23),
1141 11641-11646. doi: 10.5194/acp-10-11641-2010
- 1142 Stephens, G., Winker, D., Pelon, J., Trepte, C., Vane, D., Yuhas, C., ... Lebsock,

- 1143 M. (2018). Cloudsat and calipso within the a-train: Ten years of actively
 1144 observing the earth system. *Bull. Amer. Meteor. Soc.*, *99*(3), 569-581.
- 1145 Stephens, G. L. (2005). Cloud feedbacks in the climate system: A critical review. *J.*
 1146 *Climate*, *18*(2), 237-273.
- 1147 Stephens, G. L., Li, J., Wild, M., Clayson, C. A., Loeb, N., Kato, S., ... Andrews,
 1148 T. (2012). An update on earth s energy balance in light of the latest global
 1149 observations. *Nat. Geosci.*, *5*(10), 691.
- 1150 Stevens, B., Acquistapace, C., Hansen, A., , & Coauthors incl. Senf, F. (2020).
 1151 Large-eddy and storm resolving models for climate prediction the added
 1152 value for clouds and precipitation. *J. Meteor. Soc. Japan.* doi: 10.2151/
 1153 jmsj.2020-021
- 1154 Stevens, B., Giorgetta, M., Esch, M., Mauritsen, T., Crueger, T., Rast, S., ...
 1155 Roeckner, E. (2013). Atmospheric component of the mpi-m earth system
 1156 model: Echam6. *J. Adv. Model. Earth Syst.*, *5*(2), 146-172.
- 1157 Stevens, B., Satoh, M., Auger, L., Biercamp, J., Bretherton, C. S., Chen, X., ...
 1158 Klocke, D. (2019). Dyamond: the dynamics of the atmospheric general cir-
 1159 culation modeled on non-hydrostatic domains. *Prog. Earth Planet Sci.*, *6*(1),
 1160 61.
- 1161 Tegen, I., Hollrig, P., Chin, M., Fung, I., Jacob, D., & Penner, J. (1997). Con-
 1162 tribution of different aerosol species to the global aerosol extinction optical
 1163 thickness: Estimates from model results. *J. Geophys. Res. Atmos.*, *102*(D20),
 1164 23895-23915.
- 1165 Thomas, M. A., Devasthale, A., Koenigk, T., Wyser, K., Roberts, M., Roberts, C.,
 1166 & Lohmann, K. (2018). A statistical and process oriented evaluation of cloud
 1167 radiative effects in high resolution global models. *Geosci. Model Dev. Discuss.*,
 1168 *2018*, 1–30. doi: 10.5194/gmd-2018-221
- 1169 Tiedtke, M. (1989). A comprehensive mass flux scheme for cumulus parameteriza-
 1170 tion in large-scale models. *Monthly Weather Review*, *117*(8), 1779–1800.
- 1171 Vanni ere, B., Demory, M.-E., Vidale, P. L., Schiemann, R., Roberts, M. J., Roberts,
 1172 C. D., ... Senan, R. (2019). Multi-model evaluation of the sensitivity of
 1173 the global energy budget and hydrological cycle to resolution. *Climate Dyn.*,
 1174 *52*(11), 6817–6846.
- 1175 Voigt, A., Albern, N., & Papavasileiou, G. (2019, May). The Atmospheric Path-
 1176 way of the Cloud-Radiative Impact on the Circulation Response to Global
 1177 Warming: Important and Uncertain. *J. Climate*, *32*(10), 3051-3067. doi:
 1178 10.1175/JCLI-D-18-0810.1
- 1179 Voigt, A., & Shaw, T. A. (2015, Feb). Circulation response to warming shaped by
 1180 radiative changes of clouds and water vapour. *Nat. Geosci.*, *8*(2), 102-106. doi:
 1181 10.1038/ngeo2345
- 1182 Voigt, A., & Shaw, T. A. (2016, Dec). Impact of Regional Atmospheric
 1183 Cloud Radiative Changes on Shifts of the Extratropical Jet Stream in
 1184 Response to Global Warming. *J. Climate*, *29*(23), 8399-8421. doi:
 1185 10.1175/JCLI-D-16-0140.1
- 1186 Webb, M. J., Lock, A. P., Bretherton, C. S., Bony, S., Cole, J. N. S., Idelkadi, A., ...
 1187 Zhao, M. (2015). The impact of parametrized convection on cloud feedback.
 1188 *Phil. Trans. R. Soc. A*, *373*(2054), 20140414.
- 1189 Z angl, G., Reinert, D., R ipodas, P., & Baldauf, M. (2014). The ICon (ICosahedral
 1190 non-hydrostatic) modelling framework of dwd and MPI-m: Description of the
 1191 non-hydrostatic dynamical core. *Q.J.R. Meteorol. Soc.*, *141*(687), 563-579.
- 1192 Zelinka, M. D., Randall, D. A., Webb, M. J., & Klein, S. A. (2017). Clearing clouds
 1193 of uncertainty. *Nature Climate Change*, *7*(10), 674.